Expanding the stratigraphic record of tsunami inundation along the semi-arid, siliciclastic coast of north-central Chile

Jessica DePaolis

Thesis submitted to the faculty of the Virginia Polytechnic Institute and State University in partial fulfillment of the requirements for the degree of

Master of Science
In
Geosciences

Cristina Dura
Robert Weiss
James Spotila
Brian Romans

July 12, 2019
Blacksburg, Virginia

Keywords: North-central Chile, paleoseismology, earthquakes, tsunamis

Expanding the stratigraphic record of tsunami inundation along the semi-arid, siliciclastic coast of north-central Chile

Jessica DePaolis

ABSTRACT

On September 16, 2015, a Mw 8.3 earthquake struck offshore of the north-central Chile coast with a fault-rupture length of approximately 150 km. The earthquake triggered a tsunami that impacted 500 km of coastline from Huasco (28.5°S) to San Antonio (33.5°S), registering as much as 4.5 m on the tide gauge at Coquimbo (30.0°S) with run-up heights >10 m at a few exposed locations between Limarí (30.7°S) and Coquimbo. The tsunami provided an invaluable opportunity to examine the nature of tsunami deposit evidence in a semi-arid, siliciclastic environment, where settings suitable for the preservation of tsunami sedimentation are scarce, thereby improving our ability to identify such evidence in the geologic record. Using before-and-after-tsunami satellite imagery and post-tsunami coastal surveys, we targeted one of the few low-energy depositional terrestrial environments in the tsunami-affected area that had a high potential to preserve the 2015 tsunami deposit and older events: the Pachingo marsh in Tongoy Bay (30.3°S). We employed field and laboratory methods to document the 2015 tsunami deposit and discovered sedimentological evidence of previous tsunami inundation of the site.

The 2015 tsunami deposit and an older sand bed ~10 cm lower in the stratigraphy exhibit similar sedimentological characteristics. Both sand beds are composed of poorly to moderately sorted, gray-brown, fine- to medium-grained sand and are distinct from underlying and overlying organic-rich silty sediments. The sand beds are thinner (from ~20 cm to <1 cm) and finer (from medium- to fine-grained sand) at more inland locations, and fine upward. However, the older sand bed extends over 150 m farther inland than the 2015 tsunami deposit. To explore the differences

in the offshore ruptures that generated the tsunamis that deposited each sand bed, we employed an inverse sediment transport model (TSUFLIND). Our field survey, sedimentological data, and modeling results infer that the older sand bed preserved at the Pachingo marsh field site was produced by a larger tsunami than the 2015 tsunami. Anthropogenic evidence (copper smelter waste) along with Cs^{137} and Pb^{210} dating constrains the magnitude and age of the older sand bed to the last 130 years. Based on historical analysis of recent tsunamis that impacted the Pachingo marsh region, we infer a widespread tsunami in 1922 is the best candidate for depositing the older sand bed at our site, providing first geologic evidence of pre-2015 tsunami inundation along the north-central Chile coast.

Expanding the stratigraphic record of tsunami inundation along the semi-arid, siliciclastic coast of north-central Chile

Jessica DePaolis

GENERAL AUDIENCE ABSTRACT

On September 16, 2015 a segment of the Chilean subduction zone ruptured off the coast of north-central Chile producing a magnitude 8.3 earthquake. The earthquake created a tsunami that impacted 500 km of coastline and created waves measuring 4.5 m on the tide gauge at Coquimbo (30.0°S) with waves reaching inland to heights >10 m at a few exposed locations. The 2015 event in north-central Chile provided a unique opportunity to study tsunami deposits in semi-arid, sand-dominated environment where preservation of tsunami deposits within coastal sediments is rare, helping improve our ability to identify this type of evidence in the sedimentary record. Using before-and-after-tsunami satellite imagery and post-tsunami coastal surveys, we targeted a marsh in the tsunami-affected area that was capable of preserving the 2015 tsunami deposit and older events: the Pachingo marsh in Tongoy Bay (30.3°S). We employed field and laboratory methods to document the 2015 tsunami deposit and discovered evidence of previous tsunami overwash at the site within the sediments of the marsh. Our field work observations and sedimentary data revealed that in addition to the 2015 tsunami deposit, the site contained an older, anomalous sand bed that we infer to be a tsunami based on its similarity to the modern deposit at the site. Our modeling results suggest that the older sand bed was deposited by a tsunami larger than the 2015 tsunami. Based on historical analysis of recent tsunamis that impacted the Pachingo marsh region, we infer a tsunami in 1922 is the best candidate for depositing the older sand bed at our site. This discovery provides the first evidence of tsunami sediments from pre-2015 tsunami inundation along the north-central Chile coast.

ACKNOWLEDGEMENTS

I would first like to thank my advisor, Dr. Tina Dura, who took the biggest leap of faith by agreeing to have me as her first graduate student. I have learned more than I could have imagined and have been able to travel to the most incredible places in the name of science. Thank you, endlessly, for introducing me to the world of paleoseismology. Thanks for believing in me, for pushing me to be a better scientist, and for being a great mentor and friend throughout this crazy, one-year process.

To my committee members: Dr. Jim Spotila, Dr. Brian Romans, and Dr. Robert Weiss. Thank you all for being supportive and encouraging throughout this process. With your guidance and suggestions my thesis project has become more evolved and thorough with time. It has helped me to have new perspectives and grow as a scientist.

I extend my thanks to colleagues who have helped immensely in this process: Ben Gill, Marco Cisternas, Reide Corbett, Lisa Ely, Hui Tang, and countless others. Without them as teachers and sound boards I would be lost.

Lastly, I would like to thank my parents for their constant encouragement, my sisters for always being a phone call away, my friends for being the best supporters, and to Shaun White for his wonderful company. This achievement would not have been possible without their love and kindness.

TABLE OF CONTENTS

1. INTRODUCTION

The north-central Chile coast lies along a seismically active portion of the Chilean subduction zone between 30˚S and 32˚S that has produced multiple >M8 earthquakes over the last few centuries (Métois et al., 2013). The most recent earthquake in north-central Chile occurred in 2015 (Mw 8.3) and produced a tsunami that affected 500 km of coastline from Huasco (28.5° S) to San Antonio (33.5° S) (Fig. 1). The highest tsunami run-ups (~10 m) were recorded near Totoral (31° S), adjacent to the area of largest coseismic slip (Barnhart et al., 2016; Contreras-Lopez et al., 2016). Historical records document previous earthquakes with similar rupture extents in AD 1880 and 1943 that produced ground shaking in the region, but only produced low tsunamis (<4 m) (Lomnitz, 1970). The most recent significant tsunami documented in historical records in north-central Chile was in AD 1922, when a rupture to the north caused a 5-9 m tsunami that affected 400 km of coastline from Huasco to Caldera (27˚S) (Lomnitz, 1970; Carvajal et al., 2017a). Despite the historical accounts of recent seismicity in north-central Chile, records are sparse and often incomplete, leaving questions about the variability in past rupture location and length, and the varying size of tsunamis accompanying past ruptures (Dura et al., 2015). In order to assess hazards thoroughly along the north-central Chile coast, we must identify how often offshore ruptures and their accompanying tsunamis occur in the region, requiring us to investigate the geologic record to extend earthquake and tsunami histories back in time.

Paleoseismic methods can be employed to produce geologic datasets of earthquakes and tsunamis on centennial and millennial timescales, capturing rare but potentially catastrophic events and improving our ability to assess subduction zone hazards. Coastal sedimentary sequences in low-energy depositional environments can record sudden changes in relative sea level (RSL) associated with coseismic and interseismic deformation of the coast, often in combination with

widespread sand beds deposited by tsunamis accompanying large subduction zone earthquakes (Plafker and Savage, 1970; Atwater, 1987). Anomalous sand beds deposited by tsunamis can also be preserved onshore in the absence of evidence of vertical deformation of the coast, depending on the proximity of the earthquake source to the coastline and the coastal morphology and depositional environments of the region (Kelsey et al., 2002; Cisternas et al., 2005; Satake and Atwater, 2007; Dura et al., 2017). Paleoseismic studies have documented stratigraphic evidence of great subduction zone earthquakes in tidal marshes in south (Cisternas et al., 2005, 2017; Garrett et al., 2015), south-central (Ely et al., 2014; Dura et al., 2017; Hong et al., 2017), and central (Dura et al., 2015) Chile enabling the development of earthquake histories over multiple earthquake cycles. However, in north-central Chile, the combination of a semi-arid environment, rocky coastline dominated by siliciclastic sediments, and net Holocene emergence has resulted in limited low-energy depositional environments in which to preserve sedimentary evidence of coseismic deformation or tsunami inundation (Spiske et al., 2013; Soto et al., 2014; Dura et al., 2017). Due to these limitations, the 2015 tsunami provided an invaluable opportunity to investigate the geologic signature of tsunami inundation along the coastline of north-central Chile, thereby improving our ability to identify such evidence in the geologic record.

Here, we present the first stratigraphic evidence of pre-2015 tsunami inundation along the coast of north-central Chile. Using the stratigraphic and sedimentological characteristics of the 2015 tsunami deposit as comparison, we identified previous tsunami inundation in one of the few low-energy depositional environments along the north-central Chile coast, the Pachingo marsh (30.5˚S). Our detailed sedimentological, dating (Cs^{137} and Pb^{210}), geochemical, and historical analyses, and sediment transport modeling suggest that the older sand bed preserved at the Pachingo marsh was deposited by a tsunami larger than the 2015 event. Our discovery gives us

additional insight into the recurrence of high tsunamis along the north-central coast, improving our ability to assess hazards that pose a threat to coastal communities.

2. TECTONIC AND COASTAL SETTING

2.1 Past earthquakes and tsunamis

The Chilean subduction zone extends 3500 km, marking the plate boundary between the Nazca plate and the South American plate (Fig. 1). In north-central Chile, the Nazca plate subducts at an angle of 10-20˚ at a rate of 68-80 mm/yr (Pardo et al., 2002; Métois et al., 2013; Dura et al., 2015). Geodetic studies show that our study site at the Pachingo marsh lies within a highly coupled portion of the subduction zone between ~30˚S and ~34˚S defined as the Metropolitan segment (Métois et al., 2013). Within the Metropolitan segment, two peaks of higher coupling indicate two asperities in the south and north separated by a zone of lower coupling at ~32 ˚S. Each asperity has experienced recent ruptures in AD 1906 and 1985 (southern) and 1943 and 2015 (northern). Also within the Metropolitan segment, two major bathymetric features approximately coincide with regions of lower coupling to the north (Challenger Fracture Zone, 30˚S) and to the south (Juan Fernandez Ridge, ~32˚S; Métois et al., 2013; Tilmann et al., 2016). These subducting seafloor features have been discussed as possible controls on rupture propagation, however recent ruptures in the region, including the 2015 north-central Chile earthquake, did not extend as far north or south as these features (Tilmann et al., 2016).

Based on historical accounts and modern observations, the three most recent large ruptures within the northern portion of the Metropolitan segment occurred in 1880 (M= ~7.7), 1943 (Mw= 7.9), and 2015, (Mw= 8.3; Fig. 1; DeMets et al., 1994; Beck et al., 1998; Heinze, 2003; Saillard et al., 2009; Métois et al., 2013; Soto et al., 2014; Barnhart et al., 2016). Of the earthquakes to affect the northern portion of the Metropolitan segment, the 2015 event produced the highest (>10 m) run ups and most widespread tsunami, although it is difficult to evaluate tsunami run-up heights for older events due the sparsely populated coast in this region (Lomnitz, 1970; Contreras-Lopez

et al., 2016). Historical accounts indicate that previous tsunamis comparable to the 2015 event impacted north-central Chile in AD 1730 and 1922, but they were produced by ruptures mainly focused to the south (1730, M= ~8.5; Lomnitz, 1970) and the north (1922, M = 8.5-8.6; Fig. 1; Métois et al., 2013; Carvajal et al., 2017).

2.2 Strategies and challenges for identifying tsunami sediments

Reconstructing the history of tsunami inundation along subduction zone coastlines is based on the identification of anomalous sand beds in low-energy depositional environments such as salt and freshwater marshes, interdunal swales, and coastal lakes and lagoons. Through the study of numerous modern tsunami analogues worldwide, field studies of tsunami deposits have become more detailed and complex over the last decade (e.g., Bourgeois et al., 1999; Gelfenbaum & Jaffe, 2003; Minoura et al., 1997; Shi et al., 1995). This has advanced research on tsunami deposits from studies prior to the 2004 Sumatra tsunami that focused on general deposit mapping and limited grain size analysis (e.g., Shi et al., 1995) to a more refined approach that uses high-resolution grain size measurements and sediment transport modeling (e.g. Morton et al., 2007) to characterize tsunami events.

When a tsunami is triggered by a seismic event, long period tsunami waves transport offshore marine sediment and debris to landward depositional areas (Switzer and Jones, 2008). Heavy erosion to the beach, dunes, and berms along the immediate shoreline is expected, providing the source sediment for the overwash. Tsunamis transport near-shore sediment in suspension, producing laterally extensive sand deposits with upward fining, and landward thinning and fining characteristics (Morton et al., 2007; Switzer and Jones, 2008). High-energy tsunami inundation and sediment deposition usually creates distinctive contacts with underlying, pre-tsunami

sedimentary layers with characteristics such as sharp or eroded lower contacts, anomalous marine sediments, and rip-up clasts (Switzer and Jones, 2008).

Tsunami deposit preservation and identification is most clear in low-energy depositional environments composed of fine-grained sediments and covered in vegetation, where anomalous coarse-grained overwash sediments can be quickly covered and protected from erosional surface processes (Gleason et al., 1979; Morton et al., 2011; Spiske et al., 2013). In such environments, modern and paleotsunami deposits can be easily distinguished from underlying and overlying organic, fine-grained sediment. In semi-arid and arid climates dominated by siliciclastic sediment, limited low-energy depositional environments make preserving and identifying tsunami deposits challenging. Sand-dominated estuaries and lowlands with sparse vegetation typical of such regions do not provide the accommodation space necessary to bury and preserve tsunami sediments. Any coarse-grained overwash sediments that do get preserved are difficult to distinguish from underlying and overlying sandy sediments in the stratigraphic record (Switzer and Jones, 2008). Strategies for identifying tsunami deposits in semi-arid and arid climates dominated by siliciclastic sediment include targeting coastal lakes and lagoons, interdunal swales, and marshy, vegetated areas along the coast that may provide the necessary accommodation space to preserve overwash sediment (Jankaew et al., 2008).

Additional challenges in tsunami deposit identification in open coastal settings include distinguishing anomalous coarse-grained tsunami sediment from storm overwash and fluvial sediments (Foster et al., 1991; Minoura and Nakaya, 1991; Bryant et al., 1992; Nelson et al., 1996; Switzer and Jones, 2008). Storm overwash deposits are composed of anomalous marine sand, exhibit landward fining and thinning, and are laterally continuous, all characteristics of tsunami overwash deposits (Minoura and Nakaya, 1991; Shi et al., 1995; Dawson et al., 1996; Gelfenbaum

and Jaffe, 2003; Kortekaas and Dawson, 2007; Morton et al., 2007). Both storms and tsunamis have been known to extend several kilometers inland, arguing that the inland extent of anomalous sand beds is also not a diagnostic criterion for determining the difference between them (Nott, 2003). One major distinguishing feature to determine the difference between tsunamis and storm deposits is the lower contact with underlying sediment. Tsunamis can create sharp (<1-3 mm) but erosive contacts with pre-tsunami sediment often with rip-up clasts present, while storm overwash sediments create a sharp contact, but fail to cause erosion to the underlying layer (Minoura and Nakaya, 1991; Nanayama et al., 2000; Dawson and Stewart, 2007).

Ephemeral streams and rivers, common to semi-arid climates, have the potential to undergo flooding events due to extensive run-off from the highlands where the rivers are sourced, creating flood deposits in coastal lowlands that may be confused with tsunami deposits (Keefer and Moseley, 2004; Spiske et al., 2013). However, these fluvially-sourced deposits are generally much smaller overwash deposits, have finer grain size, and not laterally continuous than their storm and tsunami overwash counterparts. Moreover, fluvial deposits do not contain landward fining and thinning characteristics and they do not include anomalous marine sediment making them easy to distinguish from a true tsunami deposit (Switzer and Jones, 2008).

2.3 Tongoy Bay and Pachingo marsh

The north-central Chile coastline exhibits variable shore morphologies consisting of ephemeral alluvial valleys and associated estuaries bordered by rocky headlands. Bordering Tongoy Bay, a series of tectonically elevated Pleistocene and Holocene marine terraces and beach ridges are bisected by ephemeral stream valleys (Ota and Paskoff, 1993; Soto et al., 2014). There are five terraces (6 ka, 123 ka, 232 ka, 321 ka, and 690 ka; Fig. 2a) within the field site that formed within the last 700 ka years related to periods of rapid tectonic uplift (Ota and Paskoff, 1993;

Saillard et al., 2009; May et al., 2013). The steep valleys draining to Tongoy Bay are created by the net tectonic uplift of the coast from movement along the subduction zone. Additionally, a secondary fault system (Puerto Aldea Fault and the Pachingo Fault) tectonically raises the approximately 100 km^2 central lowland (Tongoy Paleobay) and promotes the valleys' incision into the marine terraces (Le Roux et al., 2006; Soto et al., 2014). The semi-arid climate of north-central Chile is characterized by prolonged multi-year droughts or extremely rainy seasons, which can cause flooding and debris flows in river and ephemeral stream valleys causing further incision (Pfeiffer et al., 2011; Soto et al., 2014). The Tongoy Paleobay is composed of Miocene-Pleistocene units (mudstones, sandstones, coquina, and conglomerates) interpreted as bay-fill sediments of the Coquimbo Formation formed during a series of transgressions and regressions related to tectonic and regional RSL changes (Le Roux et al., 2006; Soto et al., 2014).

We focus our study in the Pachingo marsh (30.30°S, 71.75˚W) in southern Tongoy Bay, one of the few low-energy, fine-grained, vegetated depositional environments in the region with the potential to preserve tsunami sediments (Fig. 2). The Pachingo marsh lies ~100 m from the coast at ~0.8 m elevation and is composed of fine-grained organic silts covered by dense salt-marsh vegetation (*Salicornia* sp.). The marsh and beach are separated by a ~2.0 m-high beach berm and coastal road that runs parallel to the shoreline about ~75 m from the coast. To the west of the marsh, the ephemeral Pachingo River flows south to north. The river is sourced by the coastal range that sits ~30 km inland, but because rainfall is very low in this region (~7.0 cm of annual rainfall) the river pools west of our field site behind the coastal berm and does not ordinarily reach Tongoy Bay (Soto et al., 2014). The modern Tongoy Bay is wave dominated and microtidal (Great Diurnal tidal range of 1.5 m between MLLW-MHHW) as measured by the Chilean Hydrographic and Oceanographic service (SHOA) at Coquimbo.

2.4 September 16, 2015 tsunami effects at the Pachingo marsh

On September 16, 2015, 500 km of the north-central Chilean subduction zone ruptured triggering a tsunami that affected the coast between the cities of Huasco and San Antonio (Contreras-Lopez et al., 2016). At Pachingo, the tsunami eroded much of the modern beach and berm and created a large overwash deposit on the marsh (Fig. 3). The tsunami transported and deposited sediment in a landward thinning sheet with thickness ranging from ~20 cm near the coastal road to <1 cm roughly ~225 m inland. Aerial photos show that post-tsunami the coastal road was indistinguishable from the erosion and there was heavy overwash into the marsh (Fig. 4). The rooted marsh vegetation was strong enough to withstand the event, but was folded inland parallel to tsunami flow direction. Multiple waves were recorded, but none were observed due to evacuation of the coastal area after the earthquake (Contreras-Lopez et al., 2016). The first wave arrived shortly after low tide and secondary waves sustained significant amplitudes for almost one full tidal cycle (Contreras-Lopez et al., 2016). The erosion at the mouth of the Pachingo River removed enough sediment to connect the river and Tongoy Bay for a short time (~4-6 weeks) before the coast recovered.

2.5 August 8, 2015 storm effects along the central coast of Chile

During El Niño events, open coastal settings along the Pacific coast of Chile are susceptible to large surges. Waves may reach 5-6 m on average during these events (May et al., 2013). On August 8, 2015 a storm coinciding with high tide created a large surge along ~500 km of coast between Coquimbo (30.0˚S) and Bucalemu (34.5˚S). Abnormally high (10 m) waves and high (~110 km/h) winds produced deadly flooding and extreme coastal erosion (Carvajal et al., 2017b; Bahlburg et al., 2018). However, aerial photo comparison of coastal erosion between the August 2015 storm surge and September 2015 tsunami shows that the erosion from the storm surge was

not as destructive as the tsunami (Fig. 4). However, the large storm surge potentially eroded much of the beach which made erosion from the tsunami waves more intense. This comparison suggests that even the largest observed storm surges that have affected our site are not capable of transporting sediment into the inland marsh environments.

3. APPROACH AND METHODS

In order to document the history of tsunami inundation of the Pachingo marsh, we described hand-dug pits and gouge cores at 38 locations throughout the site (Fig. 2c). Pits and gouge cores were completed in coast perpendicular and coast parallel transects to characterize the lateral extent of tsunami overwash deposition from 2015 and older sand beds. In the field, we recorded detailed descriptions of the stratigraphy including color (Munsell soil color charts, 1975), sharpness of upper and lower contacts, depth, grain size, and estimates of the proportion of sand, silt, clay, and organics using the methods by Troels-Smith (Nelson et al., 2015). We determined the locations and relative elevations of pits and cores using a differential GPS (Trimble, model R8). Elevations were then tied to a tidal datum measured with a portable acoustic tide gauge. The tide gauge was installed in Puerto Aldea on a concrete staircase at the end of a dock. It was set on 2 July, 2018 and left to record continuously for 24 hours. We used tidal predictions from the TPXO8-Atlas tidal model to match with our tide gauge observations in order to determine elevation of the tide gauge relative to local mean sea level (MSL), and tied our pit and core locations to that elevation (Egbert et al., 1994; Egbert and Erofeeva, 2002; Ely et al., 2014).

We focus the bulk of our laboratory analysis on transect (A-A'), which extends ~400 m inland from the shoreline and consists of 13 pits and cores spaced ~10-20 m apart (Fig. 2c). This transect is representative of the thickness of the 2015 tsunami overwash deposit and the underlying sediments that are throughout the Pachingo marsh. We collected sediment from locations along this transect to perform grain size, geochemical, and dating analyses in the lab. Monolith or core samples were taken from locations 2, 5, and 9 and bulk sediment samples from locations 1, 3, 4, 7, 8, 213, 214, 215, and 216. Bulk samples from anomalous sand beds were also taken from all

locations along transects B-B' and transect C-C' to explore the spatial variability of possible overwash sediments at our site.

3.1 Grain size analysis

In order to characterize the sand deposits, identify fining upward sequences commonly found within tsunami deposits, and draw comparisons between the sand deposits, we ran high-resolution grain size analysis on select locations representative of site stratigraphy (locations 2, 5, and 9), and bulk grain size analysis on the anomalous sand beds from all other locations along transect A-A' (1, 3, 4, 7, 8, 213, 214, 215, and 216) and transects B-B' and C-C'. We digested the organic material in each sample using hydrogen peroxide (30% concentration). Using a Malvern Mastersizer 3000 laser-particle size analyzer we performed grain size analysis on the remaining inorganic material for each sample (Donato et al., 2009). We use the Wentworth Phi scale for grain size and calculated statistics including mean grain size, sorting, skewness, and kurtosis using the GRADISTAT statistical software package. We further compare the grain size between the 2015 and older sand bed using D10 (the diameter where 10% of the sample's volume is comprised of smaller grains) and D90 (the diameter where 90% of the sample's volume is comprised of smaller grains).

3.2 Dating

To constrain the age of the older sand bed, we used Cesium (Cs^{137}) and Lead (Pb^{210}) dating methods. A monolith from location 5 was used for analysis because the older sand bed is thick (~5 cm) at this location and stratigraphy is representative of the characteristics of the sediments throughout the site.

As a byproduct of fission reactions, Cs^{137} ($t_{1/2}$=30.1 years) is a dateable anthropogenic radionuclide produced by hydrogen bomb testing that occurred from November 1952 until 1963.

Nuclear weapon testing added Cs^{137} to the atmosphere therefore detection of Cesium in Northern hemisphere sediments due to fallout is typical between 1953 and 1963. A similar timeline of testing is present in the Southern hemisphere, however, Cs^{137} is significantly less detectable due to reduced testing activities as compared to the northern hemisphere. Therefore, Cs^{137} can be used to date sediments ~60 years ago.

As a naturally occurring radioisotope, Pb^{210} ($t_{1/2}$=22.3 years) is a product of the Uranium-238 decay series and is continually being produced in the atmosphere and on Earth's surface (Corbett and Walsh, 2015). Uranium-238 decays to Radium-226, which produces a short-lived parent isotope Radon-222 that decays to Pb^{210}. Lead is a useful tracer for dating sediments up to 100 years (or roughly 5 Pb^{210} half-lives).

3.3 Geochemical analysis

To investigate the potential for coseismic land-level change at our site and understand general past environmental changes, we used geochemical analysis techniques to explore the organic content of the stratigraphic units. We employ total organic carbon (TOC), the ratio of organic carbon to total nitrogen (C/N), and stable organic isotopes ($\delta^{13}C$) to understand how the organic content of the silt deposits might be changing before and after the older sand bed. $\delta^{13}C$ can give insight into the paleoenvironmental conditions at a coastal site due to the large variation in the δ C13 signature provided by C3 v C4 plant species. C3 ($\delta^{13}C$ values ranging from -28‰ to -22‰) plants inhabit a more brackish to freshwater environment while C4 ($\delta^{13}C$ values ranging from -17‰ to -9‰) plants populate saltmarsh and more marine-influenced environments (Woodroffe et al., 2010).

We subsampled a core from location 9 at 2 cm resolution in homogenous sediment and at 1 cm resolution 5 cm above and below the older sand bed. From each subsampling location we transferred ~3 cc of sediment to a 50 mL centrifuge vial. Each vial was filled with ~30 mL of deionized water and a vortexer was used to completely mix the sediment and water. After mixing, the vials were placed in the centrifuge to separate water from sediment, excess water was removed, and the vials were filled with more deionized water. This process was repeated three times in order to rinse the saltwater from the sediment. Once the last vial was drained of excess water, all sample vials were placed into the oven at 50˚C until the samples were completely dried. The dried sediment was individually ground to a fine powder using a mortar and pestle to completely homogenize each sample, with careful consideration to thoroughly clean each piece of equipment between each sample to avoid cross contamination. Homogenized samples were weighed to 0.500 mg using a microbalance and each sample placed into a tin capsule and folded tightly using forceps to remove all air. The sample capsules were then placed into a mass spectrometer for analysis (Woodroffe et al., 2010).

3.4 Tsunami modeling

In order to better understand the hydrodynamics of tsunami inundation at our site and compare the 2015 tsunami deposit to older sand beds, we used an inverse sediment transport model for tsunami flow inversion of deposits (TSUFLIND). TSUFLIND is a model that takes field and laboratory observations of a known or inferred tsunami deposit as input and inversely calculates the flow speed, offshore wave amplitude, Froude number, and flow depth of the wave that created it (Tang and Weiss, 2015). For this study, we focus on the flow speed output of TSUFLIND as a means to compare the relative size of the 2015 tsunami and previous tsunamis that may have

affected our site. We ran the model on locations 1, 2, 3, 4, 5 and 7 for both the 2015 deposit our candidate older tsunami deposit.

Inputs to the model included our grain size results, topographic data, and deposit sediment thicknesses from both sand deposits along transect A-A' (Tang and Weiss, 2015). To use TSUFLIND to interpret our results, we considered several assumptions that the program requires: 1) the sediment must be deposited in suspended load (evidence of upward fining of sediment must be present), 2) there is a pattern of landward fining of the deposit sediments, and 3) the topography of the study site does not have large changes in relief (Tang and Weiss, 2015). The first assumption implies that sediments were deposited by a wave rather than a fluvial source. Waves create less friction and deposit sediment while it settles from suspension, while fluvial sources typically deposit in bedload. The second assumption implies the deposit exhibits landward fining characteristics within the sediments, a property of both storm and tsunami deposits. The third assumption is specific to the study site and implies that the topography sustains consistent elevation because any large changes in elevation between sample locations will create wave backflow calculations.

The 2015 deposit and the older sand bed were able to pass assumptions which allowed us to run TSUFLIND for both deposits independently of each other. The first and second assumptions, requiring sediments to be deposited in a suspension load and fine landward, are easily met by the 2015 tsunami deposit since these are both observable characteristics of tsunamis (Morton et al., 2007; Switzer and Jones, 2008). The third assumption assumes a relatively flat land surface with no sharp changes in topography that could affect modeling forward flow and backflow of the wave. We used locations 1, 2, 3, 4, 5, and 7 for modeling because locations beyond 7 varied too sharply in elevation. The older sand bed also met the first and second assumptions easily. Fining upwards

is specific to suspended load sediments which we observed in the sediment of the older sand bed (Morton et al., 2007). The sand bed also displayed characteristics of fining landward. To understand how topography of the Pachingo marsh has changed from modern day to the time of deposition of the older sand in order to meet the third assumption, we employed the historical maps of the site dating back to 1889. The maps were crucial in understanding the development of the geomorphology of the Pachingo marsh over the last ~150 years. We were able to observe some tributary migration, but no major changes to the landscape of the site. Therefore, we assume that the topography has not undergone significant changes between the time of deposition of the older sand bed and the deposition of the 2015 tsunami deposit. With this third assumption met we were able to proceed with using TSUFLIND to compare wave velocity of the events producing the 2015 deposit and the older sand bed.

4. RESULTS

4.1 General site stratigraphy

We observed four main lithostratigraphic units (units 1, 2, 3, 4) and two distinct, anomalous sand beds in the Pachingo marsh stratigraphy. A compact, gray basal sand (unit 1) containing very little organic material uniformly underlies the marsh sediments between 0.10 and 0.58 m MTL. The base of the basal sand is unknown, but cores and pits show that it extends well below 0.10 m. A 0.10-0.15 m thick light brown organic silt (unit 2) overlies the basal sand in most parts of the marsh. Unit 2 contains sparse humified organic matter. A 0.05-0.10 m thick brown organic silt (unit 3) overlies unit 2. It is distinguished from unit 2 by its darker color and the presence of visible plant fragments and roots (5-10 mm long). A 0.01-0.04 m thick dark brown, rooted, silty organic mat (unit 4) is found consistently at all locations in transect A-A' above the dark brown organic silt (unit 3).

We document two distinct anomalous sand beds interbedded within and above units 1-4. A laterally continuous sand bed deposited by the 2015 tsunami extends ~225 m inland and 150 m laterally and is found between 0.507 and 0.843 m MTL. The deposit varies in thickness from 20 to < 1 cm and is composed of fine- to medium-grained sand. The 2015 tsunami deposit flattened and buried the vegetated (*Salicornia* sp.) Pachingo marsh surface, creating the distinctive dark brown, rooted, silty organic mat (unit 4) described above. In the same portion of the marsh, we document an older sand bed that is interbedded within unit 2. The sand bed extends ~400 m inland and 150 m laterally and is found between 0.34 and 0.79 MTL. The older sand bed varies in thickness from 15 to < 1 cm and is composed of fine- to medium-grained sand. Both sands are distinct from their under- and over-lying units due to their absence of organics and characteristic sharp (<1-3 mm) or eroded lower contacts, larger mean grain size, and vertical fining upwards

sequences. Both sand beds fine and thin landwards and are laterally continuous over hundreds of meters. We performed detailed grain-size analysis at three locations representative of site stratigraphy (locations 2, 5, and 9) that contained both the 2015 sand deposit and the older sand bed (locations 2 and 5) and only the older sand bed (location 9) (Table 1).

We note the presence of discontinuous, silt (<6 cm) and sandy silt (<2 cm) deposits interbedded within the lower portions of unit 2 in some locations. A gray silt was observed at locations 2, 3, 4, 5, 7, and 213. A gray sandy silt was observed at location 5.

4.2 High-resolution grain size analysis

4.2.1 Location 2

The basal sediments of location 2 (0.50 - 0.51 m MTL) are composed of gray, poorly to moderately sorted, micaceous, fine- to medium-grained sand (unit 1; mean = 3.88 ϕ; D10 = 7.20 ϕ; Fig. 6) and contain little organic material. The basal sand contains large (>3 cm) whole, articulated shells as well as many fragments (<1 cm) of shells.

Between 0.50 – 0.58 m MTL, a light brown organic silt overlies the basal sand (unit 2; mean = 7.57 ϕ; D10 = 10.52 ϕ). The unit contains sparse humified organic matter with a slight increase in the organic content towards the top of the unit. A ~1 cm thick gray silt (mean = 5.52 ϕ; D10 = 8.96 ϕ) is interbedded within unit 2 at ~elevation 0.53 m MTL.

At 0.58 m MTL, a sharp contact separates unit 2 from the older sand bed, a 9 cm thick, gray-brown, poorly to moderately sorted, micaceous, fine- to medium-grained sand (mean = 1.79 ϕ; D10 = 2.56 ϕ). A lack of organic material, coarser mean grain size, and a decreased fine fraction distinguishes the older sand bed from under- and overlying sediments. Nine grain size samples taken at 1 cm vertical intervals show upward fining and an increased fine fraction towards the top of the sand bed.

A sharp contact separates the older sand bed from the overlying unit 2 at 0.67 m MTL. At 0.72 m MTL, unit 2 transitions to a brown organic silt (unit 3; mean = 7.52 ϕ; D10 = 10.33 ϕ). Unit 3 is distinguished from unit 2 by its darker color, an increase in humified organic matter, and the presence of visible plant fragments and roots (5-10 mm long).

At 0.75 m MTL, a 1 cm thick, dark brown, rooted, silty organic mat (unit 4; mean = 7.61 ϕ; D10 = 10.39 ϕ) overlies unit 3. The rooted organic mat represents the pre-2015 tsunami vegetated marsh surface.

At 0.76 m MTL, a sharp contact separates unit 4 from the 2015 tsunami deposit, a 7 cm thick, gray-brown, poorly to moderately sorted, micaceous, fine- to medium-grained sand (mean = 2.07 ϕ; D10 = 2.98 ϕ). A lack of organic material, coarser mean grain size, and a decreased fine fraction distinguishes the 2015 tsunami deposit from underlying sediments. Seven grain size samples taken at 1 cm vertical intervals show upward fining and an increased fine fraction towards the top of the sand bed.

4.2.2 Location 5

The basal sediments of location 5 (0.31 – 0.33 m MTL) are composed of gray, poorly to moderately sorted, micaceous, fine- to medium-grained sand (unit 1; mean = 2.11 ϕ; D10 = 3.50 ϕ; Fig. 7) and contain little organic material. The basal sand contains large (>3 cm) whole, articulated shells as well as many fragments (<1 cm) of shells.

Between 0.39 and 0.52 m MTL, a light brown organic silt overlies the basal sand (unit 2; mean = 6.57 ϕ; D10 = 9.64 ϕ). The unit contains sparse humified organic matter with a slight increase in the organic content towards the top of the unit. Unit 2 is interrupted by a small (2 cm thick), gray sandy silt (mean = 2.59 ϕ; D10 = 4.15 ϕ). It was only observed at location 5 in transect A-A’

as well as locations 208 and 209 within the transect B-B'. Two gray silt layers (mean = 5.04 ϕ; D10 = 8.06 ϕ) are also interbedded within unit 2 at ~0.40-0.45 m MTL and ~0.47–0.48 m MTL.

At 0.52 m MTL, a sharp contact separates unit 2 from the older sand bed, a 5 cm thick, gray-brown, poorly to moderately sorted, micaceous, fine- to medium-grained sand (mean = 1.96 ϕ; D10 = 3.32 ϕ). A lack of organic material, coarser mean grain size, and a decreased fine fraction distinguishes the older sand bed from under- and overlying sediments. Five grain size samples taken at 1 cm vertical intervals show upward fining and an increased fine fraction towards the top of the sand bed.

A sharp contact separates the older sand bed from the overlying unit 2 at 0.57 m MTL. Another ~1 cm thick gray silt is interbedded with unit 2 at 0.58 m MTL. At 0.59 m MTL, unit 2 transitions to a brown organic silt (unit 3; mean = 7.94 ϕ; D10 = 10.58 ϕ). Unit 3 is distinguished from unit 2 by its darker color, an increase in humified organic matter, and the presence of visible plant fragments and roots (5-10 mm long).

At 0.64 m MTL, a 3 cm thick, dark brown rooted, silty organic mat (unit 4; mean = 7.61 ϕ; D10 = 10.48 ϕ) overlies unit 3. The rooted organic mat represents the pre-2015 tsunami vegetated marsh surface.

At ~0.66 m MTL, a sharp contact separates unit 4 from the 2015 tsunami deposit, a ~1.5 cm thick, gray-brown, poorly to moderately sorted, micaceous, fine- to medium-grained sand (mean = 2.066 ϕ; D10 = 1.300 ϕ). A lack of organic material, coarser mean grain size, and a decreased fine fraction distinguishes the 2015 tsunami deposit from underlying sediments. Two grain size samples taken at 0.5 cm vertical intervals show upward fining and an increased fine fraction towards the top of the sand bed.

A monolith from location 5 was used for Cs^{137} and Pb^{210} dating because its stratigraphy is representative of the major sedimentary units within the Pachingo marsh.

4.2.3 Location 9

The basal sediments of location 9 (0.20 – 0.25 m MTL) are composed of gray, poorly to moderately sorted, coarse-grained silt (unit 1; mean = 5.08 ϕ; D10 = 7.25 ϕ; Fig. 8) and contain little organic material. There were no shells found within the basal sediment at this location.

Between 0.25 and 0.39 m MTL, a light brown organic silt overlies the basal sediment (unit 2; mean = 6.58 ϕ; D10 = 8.58 ϕ). The unit contains sparse humified organic matter with a slight increase in the organic content towards the top of the unit.

At 0.39 m MTL, a sharp contact separates unit 2 from the older sand bed, a 3 cm thick, gray-brown, poorly to moderately sorted, micaceous, fine-grained sand (mean = 4.47 ϕ; D10 = 8.19 ϕ). A lack of organic material, coarser mean grain size, and a decreased fine fraction distinguishes the older sand bed from under- and overlying sediments. Two grain size samples taken at 1 cm vertical intervals show upward fining and an increased fine fraction towards the top of the sand bed.

A sharp contact separates the older sand bed from the overlying unit 2 at 0.42 m MTL. At 0.48 m MTL, unit 2 transitions to a brown organic silt (unit 3; mean = 6.96 ϕ; D10 = 8.73 ϕ). Unit 3 is distinguished from unit 2 by its darker color, an increase in humified organic matter, and the presence of visible plant fragments and roots (5-10 mm long).

At 0.56 m MTL, a 4 cm thick, dark brown rooted, silty organic mat (unit 4; mean = 6.82 ϕ; D10 = 8.71 ϕ) overlies unit 3. At this location the densely rooted organic mat is at the marsh surface due to only trace amounts of the 2015 tsunami overwash deposition being present.

Location 9 was also used for geochemical analysis where sediment samples were taken at 1 cm vertical intervals.

4.3 Modern surface grain size sampling

Modern surface samples (M1–M15) collected from subtidal, beach, and beach ridge environments adjacent to the Pachingo marsh were composed of gray to gray-brown, poorly to moderately sorted, micaceous, fine- to medium- grained sand (average = 2 ϕ), with the lowest elevation subtidal and beach samples containing a higher fine-sand component compared to higher elevation beach and beach berm samples (e.g., M1 sampling location D10 = 1.222 ϕ and M13 sampling location D10 = 0.665 ϕ; Fig. 5). The mineralogy, grain size, and color of the 2015 tsunami deposit and older sand bed correspond with the modern beach sand characteristics.

4.4 Cs^{137} and Pb^{210} dating

Our Cs^{137} and Pb^{210} dating results constrain the timing of the deposition of the top ~20 cm of sediment in the Pachingo marsh to the last ~120 years (Fig. 9). We observe a peak of Cs^{137} between 4.5 and 6.5 cm depth at location 5 (sediment age ~AD 1963), with no Cs^{137} present below 8 cm (sediment age ~AD 1950). Assuming steady state accumulation in the marsh, then we can calculate an accumulation rate of ~0.12 cm/yr for the two time horizons represented by the peak in Cs^{137} and the absence of Cs^{137} in the core. Based on this accumulation rate, the top 12 cm of sediment were deposited post-AD 1920, including the older sand bed. Pb^{210} activities are low and difficult to interpret, but the presence of low-level Pb^{210} activity at 16-19 cm depth suggests that sediments above this depth were deposited after ~AD 1900.

The low amounts of Cs^{137} and minimal changes in Pb^{210} with depth made interpreting the core D10very difficult. Due to this difficulty, we used scoria found in the stratigraphy at a few locations to provide an additional constraint on the age of the sediments in the marsh. The scoria is interpreted to be sourced from a nearby copper smelter in operation between 1839 and late 1880s.

The scoria was found in and below the older sand bed giving us an initial age constraint of deposition to the mid 1800s and older.

4.5 Geochemical analysis

The geochemical results from location 9 exhibit low organic content (TOC = 0.56 wt%) and low C:N values (~5), and $\delta^{13}C$ enrichment (~-12 ‰) of the basal sediments (unit 1) at ~0.23 m MTL (Fig. 10). There is a gradual increase in TOC (~5 wt%) and C:N values (~10), and a gradual fall in $\delta^{13}C$ values (~-25 ‰) at ~0.38 m MTL, starting ~5 cm below the older sand bed. Within the older sand bed (0.40 m MTL) there is a spike in the C:N values (24) which could be reflecting the presence of woody debris (lignin) in the sand. Between ~0.54 m and ~0.57 m MTL (units 3 and 4), the highest TOC (5-10 wt%) and C:N values (~12) and the lowest $\delta^{13}C$ values (~-27 ‰) in the core. We note there are no major shifts in TOC, C:N, or $\delta^{13}C$ values across the older sand bed suggesting there is no signature of distinct environmental changes before and after sand deposition.

4.6 Tsunami modeling

We incorporated our detailed grain size results from the two anomalous sand beds present at our site into the inverse tsunami model (TSUFLIND) to calculate flow speed at locations 1-7 along Transect A-A' (Fig. 11). Both sand beds satisfied the assumptions required to apply the TSUFLIND model and were run independently of each other.

4.6.1 Flow speeds for the 2015 tsunami deposit

To establish the wave characteristics of a known tsunami inundation event first, we ran TSUFLIND for the 2015 tsunami deposit. Model output for the 2015 tsunami deposit shows a

decrease in flow speed of the wave as it moves inland from location 1 to 7. Speeds are initially ~4.8 m/s at location 1 and incrementally decrease as marsh vegetation and loss of momentum slow the wave. As the wave reaches location 4 it has already slowed to ~3.5 m/s. By the time the wave reaches location 7 it is moving at ~2.5 m/s, about half of its original speed.

4.6.2 Flow speeds for the older sand bed

Model output for the older sand bed shows a decrease in the wave flow speed as it moves inland from location 1 to 7. Speeds range from ~5 m/s at location 1, gradually losing momentum and slowing to ~4.3 m/s at location 4. When the wave reaches location 7, it has only slowed to ~3.6 m/s, more than 1 m/s faster than the speed calculated at location 7 for the 2015 tsunami. All flow speeds calculated for the older sand bed are observably higher than the speeds for the 2015 event, helping us to understand the relative comparison in strength and size of the waves that produced these sand beds.

5. DISCUSSION

5.1 Late Holocene environmental evolution of the Pachingo marsh

The stability of the Pachingo marsh over the last few centuries has made it one of the only low-energy depositional environments in north-central Chile with the potential to preserve tsunami overwash deposits. Based on our field observations, laboratory analyses, historical investigation, and previous studies at coastal sites in Tongoy Bay (Ota and Paskoff, 1993; May et al., 2013), we interpret the sedimentary sequence preserved above the basal sand as representing a shift from a marine to freshwater depositional environment in the Pachingo marsh over the last ~200 years. At the base of our locations, we observed fragmented and whole articulated shells in the basal sand that are characteristic of sublittoral environments, suggesting an open marine environment in the past. This is consistent with our geochemical results that indicate marine conditions prevailing at the base of location 9 as shown by the low organic content (TOC), low C:N values, and $\delta^{13}C$ enrichment of the basal sediments. We see a gradual transition to lower energy, brackish conditions reflected by the deposition of finer-grained material with a higher organic content, a gradual rise in TOC and C:N values, and a gradual fall in $\delta^{13}C$ values starting below the older sand bed. This gradual transition continues until maximum TOC and C:N values and minimum $\delta^{13}C$ values are observed in the top ~5 cm of core 9, reflecting the current freshwater environment of the Pachingo marsh.

The timing of the deposition of sediments typical of low-energy sedimentary environments at the Pachingo marsh is constrained by our Cs^{137} and Pb^{210} dating, the presence of scoria in the stratigraphy, and historical maps of the area (Fig. 2). Our Cs^{137} and Pb^{210} results show that sediments above the basal sand were deposited in the last ~200 years, based on sediment

accumulation rates calculated from the presence of Pb^{210} at ~20 cm depth (~AD 1890), the appearance of Cs^{137} at 8 cm depth (~AD 1950), and the Cs^{137} peak at 4.5 and 6.5 cm depth (~AD 1963). The presence of 1-3 cm diameter scoria pieces found just below, within, and above the older sand bed in the Pachingo marsh stratigraphy provide an additional maximum age constraint for the deposition of the top ~20 cm of sediment of ~AD 1870. We tracked the source of the scoria to a railroad depicted in historical maps (Fig. 2; railroad in operation starting in AD 1869) running south of the site and crossing the Pachingo River via bridge to a copper smelter waste site on northeast Tongoy Bay, which was in operation between AD 1834 – late 1880s. While this railroad does not exist today, we discovered the old train track bed with scattered railroad nails and scoria pieces where the historical maps show the railroad. We infer that the scoria was likely spilled by the train into the Pachingo marsh, and then transported across the marsh by infrequent, heavy, localized flooding or tsunami overwash events.

The historical maps depicting Tongoy bay and the Pachingo marsh in 1889-1904 and 1904-1939 show a marsh environment at our site similar to that of today for at least the last 130 years. The oldest map shows the Pachingo marsh similar to the modern marsh, however the Pachingo River connects to Tongoy Bay, suggesting that the fluvial geomorphology and coastal water influence was slightly different in the past. The main channel does not show significant differences in location, suggesting it has not migrated in the more recent past, however there are tributaries that are observed on the map, but not at the modern marsh. This observation suggests that the marsh has been influenced by fluvial channel migration in the past which may create the discontinuous coarse silt and fine sand layers similar to those that we observed in isolated locations. The map from 1904-1939 features very similar geomorphology to the current marshland. The river, like today, does not connect to Tongoy Bay, but instead pools at its terminus (Fig. 2a).

Our environmental interpretations and our inferences about the timing of sediment deposition in the Pachingo marsh are consistent with the findings of (May et al., 2013) that reported geochemical evidence showing marine mollusks present in the basal sand at a site ~50 m east of the Pachingo marsh, followed by a gradual transition to a brackish and then freshwater environment. Radiocarbon ages from the basal sand presented by (May et al., 2013) and from the most seaward beach ridge east of our coring site presented by (Ota and Paskoff, 1993) suggest that there was a seaward shift of the shoreline of ~100 m after 500 cal yr BP. This shoreline shift initiated brackish, back-barrier conditions and eventually the freshwater conditions that exist in the Pachingo marsh today (May et al., 2013).

We infer that the seaward shift and progradation of the shoreline over the last ~500 years occurred due to net local RSL fall during that time period driven by RSL fall following the mid-Holocene sea level highstand (Dura et al., 2015) and slow tectonic uplift of the coast (Ota and Paskoff, 1993). It has also been suggested that periodic punctuated uplift along the coast caused by earthquakes in the late Holocene may have contributed to the seaward shift of the shoreline (May et al., 2013), but we do not find evidence of sudden coastal uplift in the Pachingo marsh stratigraphy; the geochemical changes we observe are gradual and not associated with sand bed deposition, suggesting they are not driven by coseismic deformation.

5.2 Evidence for tsunami inundation

The 2015 event provided an opportunity for establishing the characteristics of tsunami deposition at the Pachingo marsh and acted as an example for comparing the older sand bed. Based on the similarities observed in grain size characteristics between the 2015 tsunami deposit and the older sand bed, we infer a tsunami origin for the older sand bed at our site in the Pachingo marsh. Both sand beds were composed of anomalous marine sand, contained little to no organic material,

displayed sharp or erosive lower and upper contacts, were similar in composition to the modern beach surface sediment, were laterally continuous, thinned landward, and fined upward and landward.

We observed the 2015 tsunami deposit and the older sand bed as fine-grained, micaceous, anomalous sands that are distinct from the over- and underlying sediment due to lack of organic content. The lower contacts of these sand beds are consistent with a sudden event rather than a gradual transition of environment. Comparison of the grain size shows a similarity in mean of both deposits which also matches the mean of the modern surface samples collected (Fig. 5). This match suggests that the anomalous marine sand from both deposits were sourced by the subtidal, beach, and beach ridge environments that were eroded and subsequently transported into the Pachingo marsh. Both sand beds are laterally continuous and exhibit fining upward and fining and thinning landward trends typical of tsunami and storm deposits rather than fluvial origin (Switzer and Jones, 2008). We consider the possibility of the older sand bed being deposited by a storm surge, but because the older sand bed extends ~175 m past the extent of the 2015 tsunami deposit, and one of the largest storms to affect the Chilean coast (section 2.5) in August 2015 did not inundate the marsh, we infer sand deposition by a storm surge is unlikely in the Pachingo marsh (Fig. 4). This is further supported by historical maps that depict a similar geomorphology of the lowland for at least the last 130 years, suggesting any storm surges over that time had similar difficulty in breaching the coastal beach ridges and inundating the marsh.

We infer that the discontinuous, thin coarse silt and fine-grained sand deposits found below and just above the older sand bed in stratigraphy at locations 2, 3, 4, 5, 7, and 213 were produced by storms and/or channel migration at our site. These small (<3 cm thick) layers are not part of the

anomalously coarse, laterally continuous sand beds we document and are similar in composition to sediments in the current Pachingo River channel.

5.3 Relative size of the tsunamis preserved at the Pachingo marsh

To determine the relative size of the waves that deposited the inferred tsunami sands preserved in the Pachingo marsh, we used our field, laboratory, and modeling results to compare the characteristics of the deposits (Table 2). Our field observations show that the older sand bed is thicker, extends farther inland, and covers a wider area of the marsh. Our detailed grain size analysis shows that the older sand bed is coarser at all but one location. These observations suggest that a larger wave compared to the 2015 tsunami deposited the older sand bed preserved at the Pachingo marsh.

Our inverse modeling results support our interpretation of the older sand bed being deposited by a larger wave at our site. Model results show that waves producing both the 2015 deposit and the older sand bed were faster towards the coast and slowed as they progressed inland. This characteristic is typical of a tsunami wave and is the principal process for depositing sediments in suspension. However, the flow speeds associated with the deposition of the older sand bed are faster than the flow speeds associated with the 2015 tsunami deposit. This result suggests that the tsunami that deposited the older sand bed in the Pachingo marsh was larger than the 2015 tsunami.

5.4 Constraining possible earthquake candidates with historic evidence

Based on our maximum scoria-derived age for the deposition of the older sand bed (~AD 1870), and the age constraint for the older sand bed (>AD 1920) calculated from the appearance and peak of Cs^{137} activity, we consider north-central Chile tsunamigenic earthquakes in AD 1880, 1922, and 1943 as the best candidates for depositing the older sand bed at our site (Fig. 12). We also consider the earthquake and tsunami in AD 1730 as a candidate because it was a large, regional

event that impacted the Tongoy Bay area, although it is likely too old to have deposited the older sand bed.

Tsunamigenic north-central Chile earthquakes in 1880 and 1943 had similar north-south rupture extents to the 2015 north-central Chile earthquake. The August 1880 Illapel earthquake (M 7.5 to 8) caused some minor damage to cities in north-central Chile, but major damage was focused on cities south of Tongoy Bay (Lomnitz, 1970). There were reports of a low (<4 m) tsunami produced by this event, but accounts are sparse and limited to the Coquimbo area. The historical accounts, and our dating results that suggest that the older sand bed was likely deposited post-AD 1920 suggest that the 1880 earthquake is an unlikely source for the deposition of the older sand bed.

Damage from the AD 1943 (Mw 7.9) earthquake was focused further north than the 1880 earthquake, and the low tsunami associated with the earthquake was more widespread, making it a better candidate for the deposition of the older sand bed than 1880 (Lomnitz, 1970; Beck et al., 1998; Soto et al., 2014). The 1943 rupture is remarkably similar in north-south rupture extent to the 2015 earthquake that produced a significant tsunami at our site. However, beyond the lateral rupture pattern similarities, there are major differences that set these events apart. One major difference is that the moment calculated for the 1943 event (6 x 1020 Nm; Beck et al., 1998) is ~4x smaller than the 2015 event (Tilmann et al., 2016; Carrasco et al., 2019). Tilmann et al. (2016) suggest that the 1943 and 2015 earthquakes had similar down-dip, deep slip, but that the 1943 did not rupture the shallower section of the subduction zone, and as a result had a smaller moment and produced a smaller tsunami than the 2015 earthquake (Tilmann et al., 2016; Carrasco et al., 2019). Because historical accounts show that the 1943 earthquake produced a smaller tsunami than the 2015 earthquake in the Tongoy Bay region, it is unlikely that it produced the older sand bed at our

site, which extends further inland than the 2015 tsunami deposit. For this reason, we exclude the 1943 tsunami as a candidate for the deposition of the older sand bed.

The AD 1730 Valpariso earthquake (M ~8.5) caused earthquake damage and produced a high (>4 m) tsunami along roughly 1000 km of coastline from Copiapo (27.4˚) to Concepcion (36.8˚), with most of the damage focused south of Tongoy Bay (Lomnitz, 1970; Udías et al., 2012; Dura et al., 2015). Considering that this event was one of the strongest to produce a tsunami that affected the north-central Chile coast, it became a candidate for depositing the older sand bed at our site. However, because this event is older than our maximum age of ~AD 1870 and significantly older than the sediment surrounding the older sand bed, we suggest it is not a likely candidate.

The AD 1922 northern Chile earthquake (M 8.5-8.6) produced strong shaking and a high tsunami along 400 km of the coast from Chañaral (26.3°S) to La Serena (30.0°) (Carvajal et al., 2017a). Wave heights were estimated to be between 5 and 7 m above high tides at Caldera and 9 m in Chañaral. Wave heights at Coquimbo Bay, 40 km north of Tongoy Bay, were estimated to be about 7 m above mean sea level (Lomnitz, 1970; Carvajal et al., 2017a). In comparison, wave heights at Coquimbo during the 2015 tsunami were measured at ~4.5 m above mean sea level and run-up heights were measured at ~7 m above mean sea level. Because the AD 1922 earthquake produced a tsunami larger than the 2015 tsunami at a location just 40 km away from our site in Tongoy Bay, and the timing of the tsunami is consistent with our Cs^{137} and Pb^{210} dating results that suggest the older sand bed was deposited post-1920, we consider the AD 1922 tsunami to be the best candidate for the deposition of the older sand bed at our site.

6. CONCLUSION

We characterized the 2015 tsunami deposit at the Pachingo marsh and used its signature to identify one instance of prior tsunami inundation using stratigraphy, lithology, Cs^{137} and Pb^{210} dating, geochemical analysis, historical maps, tsunami modeling. By targeting one of the few low energy depositional environments in north-central Chile to be affected by known tsunami inundation during the 2015 event, we were able to successfully identify past inundation on the north-central coast, providing a longer record of inundation hazards that may affect this coastline. Similar to the 2015 tsunami deposit, we observed anomalous marine sand, a fining upward sequence within the deposit, fining landward, and a laterally extensive sand sheet at a consistent depth in stratigraphy throughout our site, helping identify the lower sand bed as a tsunamigenic earthquake. We rule out the possibility of this being deposited by a large storm surge due to aerial photo comparisons of erosion from the storm versus the tsunami and deposit sedimentary characteristics. Furthermore, the tsunami deposit in 2015 extended inland ~225 m while the older sand bed extends inland ~400 m. This ~175 m difference in inland extent is very unlikely for a storm surge at this site and further implies it could have been created by a tsunami. We compared the speed of the waves from both events using the tsunami inverse modeling program, TSUFLIND, to show that the flow speed for the older event was faster than the 2015, suggesting it was produced by a stronger tsunami at the Pachingo marsh. Cs^{137} dates place the age of the older sand bed to be in line with the AD 1922 earthquake and large tsunami. These results are consistent with historical evidence showing that the largest, most destructive tsunami to inundate the north-central coast prior to 2015 was the 1922 tsunami.

Our interpretations are important for earthquake and tsunami hazard assessment along the coast of north-central Chile. Due to the lack of preserved tsunami deposits in this region, hazard

assessments for the north-central coast have been limited by sparse historical records. Our results show that ruptures to the north of our study site (e.g., AD 1922) can produce larger tsunamis in Tongoy Bay than ruptures immediately offshore (e.g., 2015). Thus, hazard maps that focus on potential tsunami run-ups from ruptures adjacent to the north-central Chile coast may be underestimating inundation hazards. With the addition of the 1922 tsunami to the geologic record of tsunami inundation in this region, tsunami hazards assessments in this area can be improved.

REFERENCES

Atwater, B.F., 1987, Evidence for Great Holocene Earthquakes along the Outer Coast of: Source: Science, New Series, v. 236, p. 942–944, http://www.science.earthjay.com/instruction/chemeketa/research_paper/atwater_1987_holocene_earthquakes_washington.pdf.

Bahlburg, H., Nentwig, V., and Kreutzer, M., 2018, The September 16, 2015 Illapel tsunami, Chile – Sedimentology of tsunami deposits at the beaches of La Serena and Coquimbo: Marine Geology, v. 396, p. 43–53, doi:10.1016/j.margeo.2016.12.011.

Barnhart, W.D., Murray, J.R., Briggs, R.W., Gomez, F., Miles, C.P.J., Svarc, J., Riquelme, S., and Stressler, B.J., 2016, Coseismic slip and early afterslip of the 2015 Illapel, Chile, earthquake: Implications for frictional heterogeneity and coastal uplift: Journal of Geophysical Research: Solid Earth, p. 6172–6191, doi:10.1002/2016JB013124.Received.

Beck, S., Barrientos, S., Kausel, E., and Reyes, M., 1998, Source characteristics of historic earthquakes along the central Chile subduction zone: Journal of South American Earth Sciences, v. 11, p. 115–129, doi:10.1016/S0895-9811(98)00005-4.

Bourgeois, J., 1999, Geologic Setting, Field Survey and Modeling of the Chimbote, Northern Peru, Tsunami of 21 February 1996, *in* Seismogenic and Tsunamigenic Processes in Shallow Subduction Zones,.

Bryant, E.A., Young, R.W., and Price, D.M., 1992, Evidence of Tsunami Sedimentation on the Southeastern Coast of Australia: The Journal of Geology, v. 100, p. 753–765.

Carrasco, S., Ruiz, J.A., Contreras-Reyes, E., and Ortega-Culaciati, F., 2019, Shallow intraplate seismicity related to the Illapel 2015 Mw 8.4 earthquake: Implications from the seismic source: Tectonophysics, v. 766, p. 205–218, doi:10.1016/j.tecto.2019.06.011.

Carvajal, M., Cisternas, M., Gubler, A., Catalán, P.A., Winckler, P., and Wesson, R.L., 2017a, Reexamination of the magnitudes for the 1906 and 1922 Chilean earthquakes using Japanese tsunami amplitudes: Implications for source depth constraints: Journal of Geophysical Research: Solid Earth, v. 122, p. 4–17, doi:10.1002/2016JB013269.

Carvajal, M., Contreras-López, M., Winckler, P., and Sepúlveda, I., 2017b, Meteotsunamis Occurring Along the Southwest Coast of South America During an Intense Storm: Pure and Applied Geophysics, v. 174, p. 3313–3323, doi:10.1007/s00024-017-1584-0.

Cisternas, M. et al., 2005, Predecessors of the giant 1960 Chile earthquake: Nature, v. 437, p. 404–407, doi:10.1038/nature03943.

Cisternas, M., Carvajal, M., Wesson, R., Ely, L.L., and Gorigoitia, N., 2017, Exploring the historical earthquakes preceding the giant 1960 Chile earthquake in a time-dependent seismogenic zone: Bulletin of the Seismological Society of America, v. 107, p. 2664–2675,

doi:10.1785/0120170103.

Contreras-Lopez, M. et al., 2016, Field Survey of the 2015 Chile Tsunami with Emphasis on Coastal Wetland and Conservation Areas: Pure and Applied Geophysics, v. 5, p. 299–319.

Dawson, S., Smith, D.E., Ruffman, A., and Shi, S., 1996, The Diatom Biostratigraphy of Tsunami Sediments: Examples From Recent and Middle Holocene Events: v. 21, p. 87–92.

Dawson, A.G., and Stewart, I., 2007, Tsunami deposits in the geological record: Sedimentary Geology, v. 200, p. 166–183, doi:10.1016/j.sedgeo.2007.01.002.

DeMets, C., Gordon, R.G., Argus, D.F., and Stein, S., 1994, Effect of recent revisions to the geomagnetic reversal time scale on estimates of current plate motions: Geophysical Research Letters, v. 21, p. 2191–2194, doi:10.1029/94GL02118.

Donato, S. V., Reinhardt, E.G., Boyce, J.I., Pilarczyk, J.E., and Jupp, B.P., 2009, Particle-size distribution of inferred tsunami deposits in Sur Lagoon, Sultanate of Oman: Marine Geology, v. 257, p. 54–64, doi:10.1016/j.margeo.2008.10.012.

Dura, T., Cisternas, M., Horton, B.P., Ely, L.L., Nelson, A.R., Wesson, R.L., and Pilarczyk, J.E., 2015, Coastal evidence for Holocene subduction-zone earthquakes and tsunamis in central Chile: Quaternary Science Reviews, v. 113, p. 93–111, doi:10.1016/j.quascirev.2014.10.015.

Dura, T., Horton, B.P., Cisternas, M., Ely, L.L., Hong, I., Nelson, A.R., Wesson, R.L., Pilarczyk, J.E., Parnell, A.C., and Nikitina, D., 2017, Subduction zone slip variability during the last millennium, south-central Chile: Quaternary Science Reviews, v. 175, p. 112–137, doi:10.1016/j.quascirev.2017.08.023.

Egbert, G.D., Bennett, A.F., and Foreman, M.G.G., 1994, TOPEX/POSEIDON tides estimated using a global inverse model: Journal of Geophysical Research, v. 99, p. 24821, doi:10.1029/94jc01894.

Egbert, G.D., and Erofeeva, S.Y., 2002, Efficient Inverse Modeling of Barotropic Ocean Tides: Journal of Atmospheric and Oceanic Technology, v. 19, p. 183–204.

Ely, L.L., Cisternas, M., Wesson, R.L., and Dura, T., 2014, Five centuries of tsunamis and land-level changes in the overlapping rupture area of the 1960 and 2010 Chilean earthquakes: Geology, v. 42, p. 995–998, doi:10.1130/G35830.1.

Foster, I.D.L., Albon, A.J., Bardell, K.M., Fletcher, J.L., Jardine, T.C., Mothers, R.J., Pritchard, M.A., and Turner, S.E., 1991, High energy coastal sedimentary deposits; an evaluation of depositional processes in Southwest England: Earth Surface Processes and Landforms, v. 16, p. 341–356, doi:10.1002/esp.3290160407.

Garrett, E., Shennan, I., Woodroffe, S.A., Cisternas, M., Hocking, E.P., and Gulliver, P., 2015, Reconstructing paleoseismic deformation, 2: 1000 years of great earthquakes at Chucalen,

south central Chile: Quaternary Science Reviews, p. 112–122.

Gelfenbaum, G., and Jaffe, B., 2003, Erosion and sedimentation from the 17 July, 1998 Papua New Guinea tsunami: v. 160, 1969–1999 p., doi:10.1007/s00024-003-2416-y.

Gleason, M.L., Elmer, D.A., Pien, N.C., and Fisher, J.S., 1979, Effects of Stem Density Upon Sediment Retention by Salt Marsh Cord grass, Spartina alterniflora Loisel: Estuaries, v. 2, doi:10.1007/s00442-010-1887-7.

Heinze, B., 2003, Active Intraplate Faulting in the Forearc of North Central Chile: , p. 137.

Hong, I., Dura, T., Ely, L.L., Horton, B.P., Nelson, A.R., Cisternas, M., Nikitina, D., and Wesson, R.L., 2017, A 600-year-long stratigraphic record of tsunamis in south-central Chile: Holocene, v. 27, p. 39–51, doi:10.1177/0959683616646191.

Jankaew, K., Atwater, B.F., Sawai, Y., Choowong, M., Charoentitirat, T., Martin, M.E., and Prendergast, A., 2008, Medieval forewarning of the 2004 Indian Ocean tsunami in Thailand: Nature, v. 455, p. 1228–1231, doi:10.1038/nature07373.

Keefer, D.K., and Moseley, M.E., 2004, Southern Peru desert shattered by the great 2001 earthquake: Implications for paleoseismic and paleo-El Nino-Southern Oscillation records: Proceedings of the National Academy of Sciences, v. 101, p. 10878–10883, doi:10.1073/pnas.0404320101.

Kelsey, H.M., Witter, R.C., Lettis, W., Drive, B., Creek, W., and Hemphill-haley, E., 2002, Plate-boundary earthquakes and tsunamis of the past 5500 yr, Sixes River estuary, southern Oregon — Geological Society of America Bulletin: v. 7606, p. 298–314, doi:10.1130/0016-7606(2002)114<0298.

Kortekaas, S., and Dawson, A.G., 2007, Distinguishing tsunami and storm deposits: An example from Martinhal, SW Portugal: Sedimentary Geology, v. 200, p. 208–221, doi:10.1016/j.sedgeo.2007.01.004.

Lomnitz, C., 1970, Major earthquakes and tsunamis in Chile during the period 1535 to 1955: Geologische Rundschau, v. 59, p. 938–960, doi:10.1007/BF02042278.

May, S.M., Pint, A., Rixhon, G., Kelletat, D., Wennrich, V., and Brückner, H., 2013, Holocene coastal stratigraphy, coastal changes and potential palaeoseismological implications inferred from geo-archives in Central Chile (29–32° S): Zeitschrift für Geomorphologie, Supplementary Issues, v. 57, p. 201–228, doi:10.1127/0372-8854/2013/s-00154.

Métois, M., Vigny, C., Socquet, A., Delorme, A., Morvan, S., Ortega, I., and Valderas-Bermejo, C.M., 2013, GPS-derived interseismic coupling on the subduction and seismic hazards in the Atacama region, Chile: Geophysical Journal International, v. 196, p. 644–655, doi:10.1093/gji/ggt418.

Minoura, K., Imamura, F., Takahashi, T., and Shuto, N., 1997, Sequence of sedimentation processes caused by the 1992 Flores tsunami: Evidence from Babi Island: Geology, v. 25, p. 523–526, doi:10.1130/0091-7613(1997)025<0523:SOSPCB>2.3.CO;2.

Minoura, K., and Nakaya, S., 1991, Traces of Tsunami Preserved in Inter-Tidal Lacustrine and Marsh Deposits : Some Examples from Northeast Japan Author (s): Koji Minoura and Shyu Nakaya Source : The Journal of Geology , Vol . 99 , No . 2 (Mar ., 1991), pp . 265-287 Published by : The U: The Journal of Geology, v. 99, p. 265–287.

Morton, R.A., Gelfenbaum, G., Buckley, M.L., and Richmond, B.M., 2011, Geological effects and implications of the 2010 tsunami along the central coast of Chile: Sedimentary Geology, v. 242, p. 34–51, doi:10.1016/j.sedgeo.2011.09.004.

Morton, R.A., Gelfenbaum, G., and Jaffe, B.E., 2007, Physical criteria for distinguishing sandy tsunami and storm deposits using modern examples: Sedimentary Geology, v. 200, p. 184–207, doi:10.1016/j.sedgeo.2007.01.003.

Nanayama, F., Shigeno, K., Satake, K., Shimokawa, K., Koitabashi, S., Miyasaka, S., and Ishii, M., 2000, Sedimentary differences between the 1993 Hokkaido-nansei-oki tsunami and the 1959 Miyakojima typhoon at Taisei, southwestern Hokkaido, northern Japan: Sedimentary Geology, v. 135, p. 255–264, doi:10.1016/S0037-0738(00)00076-2.

Nelson, A.R., Briggs, R.W., Dura, T., Engelhart, S.E., Gelfenbaum, G., Bradley, L.A., Forman, S.L., Vane, C.H., and Kelley, K.A., 2015, Tsunami recurrence in the eastern Alaska-Aleutian arc: A Holocene stratigraphic record from Chirikof Island, Alaska: Geosphere, v. 11, p. 1172–1203, doi:10.1130/GES01108.1.

Nelson, A.R., Shennan, I., and Long, A.J., 1996, OF GEOPHYSICAL Identifying coseismic subsidence in tidal-wetland stratigraphic sequences: Jou r nal of Geophysical Research, v. 101, p. 6115–6135.

Nott, J., 2003, Waves, coastal boulder deposits and the importance of the pre-transport setting: Earth and Planetary Science Letters, v. 210, p. 269–276, doi:10.1016/S0012-821X(03)00104-3.

Ota, Y., and Paskoff, R., 1993, Ota and Paskoff 1993 Holo SL changes N Chile.pdf: Revista Geoloica de Chile, v. 20, p. 25–32.

Pardo, M., Comte, D., and Monfret, T., 2002, Seismotectonic and stress distribution in the central Chile subduction zone: Journal of South American Earth Sciences, v. 15, p. 11–22, doi:10.1016/S0895-9811(02)00003-2.

Pfeiffer, M., Le Roux, J.P., Solleiro-Rebolledo, E., Kemnitz, H., Sedov, S., and Seguel, O., 2011, Preservation of beach ridges due to pedogenic calcrete development in the Tongoy palaeobay, North-Central Chile: Geomorphology, v. 132, p. 234–248, doi:10.1016/j.geomorph.2011.05.012.

Plafker, G., and Savage, J.C., 1970, Mechanism of the Chilean Earthquakes of May 21 and 22, 1960: Geological Society of America Bulletin, v. 81, p. 1001–1030.

Reide Corbett, D., and Walsh, J.P., 2015, ^{210}Lead and^{137}Cesium: Establishing a chronology for the last century: Handbook of Sea-Level Research, p. 361–372, doi:10.1002/9781118452547.ch24.

Le Roux, J.P., Olivares, D.M., Nielsen, S.N., Smith, N.D., Middleton, H., Fenner, J., and Ishman, S.E., 2006, Bay sedimentation as controlled by regional crustal behaviour, local tectonics and eustatic sea-level changes: Coquimbo Formation (Miocene-Pliocene), Bay of Tongoy, central Chile: Sedimentary Geology, v. 184, p. 133–153, doi:10.1016/j.sedgeo.2005.09.023.

Saillard, M., Hall, S.R., Audin, L., Farber, D.L., Hérail, G., Martinod, J., Regard, V., Finkel, R.C., and Bondoux, F., 2009, Non-steady long-term uplift rates and Pleistocene marine terrace development along the Andean margin of Chile (31°S) inferred from 10Be dating: Earth and Planetary Science Letters, v. 277, p. 50–63, doi:10.1016/j.epsl.2008.09.039.

Satake, K., and Atwater, B.F., 2007, Long-Term Perspectives on Giant Earthquakes and Tsunamis at Subduction Zones: Annual Review of Earth and Planetary Sciences, v. 35, p. 349–374, doi:10.1146/annurev.earth.35.031306.140302.

Shi, S., Dawson, A.G., and Smith, D.E., 1995, Coastal Sedimentation Associated with the December 12th, 1992 Tsunami in Flores, Indonesia, *in* Tsunamis: 1992-1994, p. 525–536.

Soto, M.V., Märker, M., Rodolfi, G., Sepúlveda, S.A., and Cabello, M., 2014, Assessment of geomorphic processes affecting the paleo-landscape of tongoy bay, Coquimbo region, central Chile: Geografia Fisica e Dinamica Quaternaria, v. 37, p. 51–66, doi:10.4461/GFDQ.2014.37.6.

Spiske, M., Piepenbreier, J., Benavente, C., and Bahlburg, H., 2013, Preservation potential of tsunami deposits on arid siliciclastic coasts: Earth-Science Reviews, v. 126, p. 58–73, doi:10.1016/j.earscirev.2013.07.009.

Switzer, A.D., and Jones, B.G., 2008, Large-scale washover sedimentation in a freshwater lagoon from the southeast Australian coast: sea-level change, tsunami or exceptionally large storm? The Holocene, v. 5, p. 787–803.

Tang, H., and Weiss, R., 2015, A model for tsunami flow inversion from deposits (TSUFLIND): Marine Geology, v. 370, p. 55–62, doi:10.1016/j.margeo.2015.10.011.

Tilmann, F. et al., 2016, The 2015 Illapel earthquake , central Chile, a type case for a characteristic earthquake? Geophysical Research Letters, v. 43, p. 574–583, doi:10.1002/2015GL066963.Received.

Udías, A., Madariaga, R., Buforn, E., Muñoz, D., and Ros, M., 2012, The large Chilean historical

earthquakes of 1647, 1657, 1730, and 1751 from contemporary documents: Bulletin of the Seismological Society of America, v. 102, p. 1639–1653, doi:10.1785/0120110289.

Woodroffe, C.D. et al., 2010, Chapter 20 Stable carbon isotope and C / N geochemistry of coastal wetland sediments as a sea-level indicator: Holocene, v. 69, p. 623–636, doi:10.1016/j.ecss.2006.04.019.

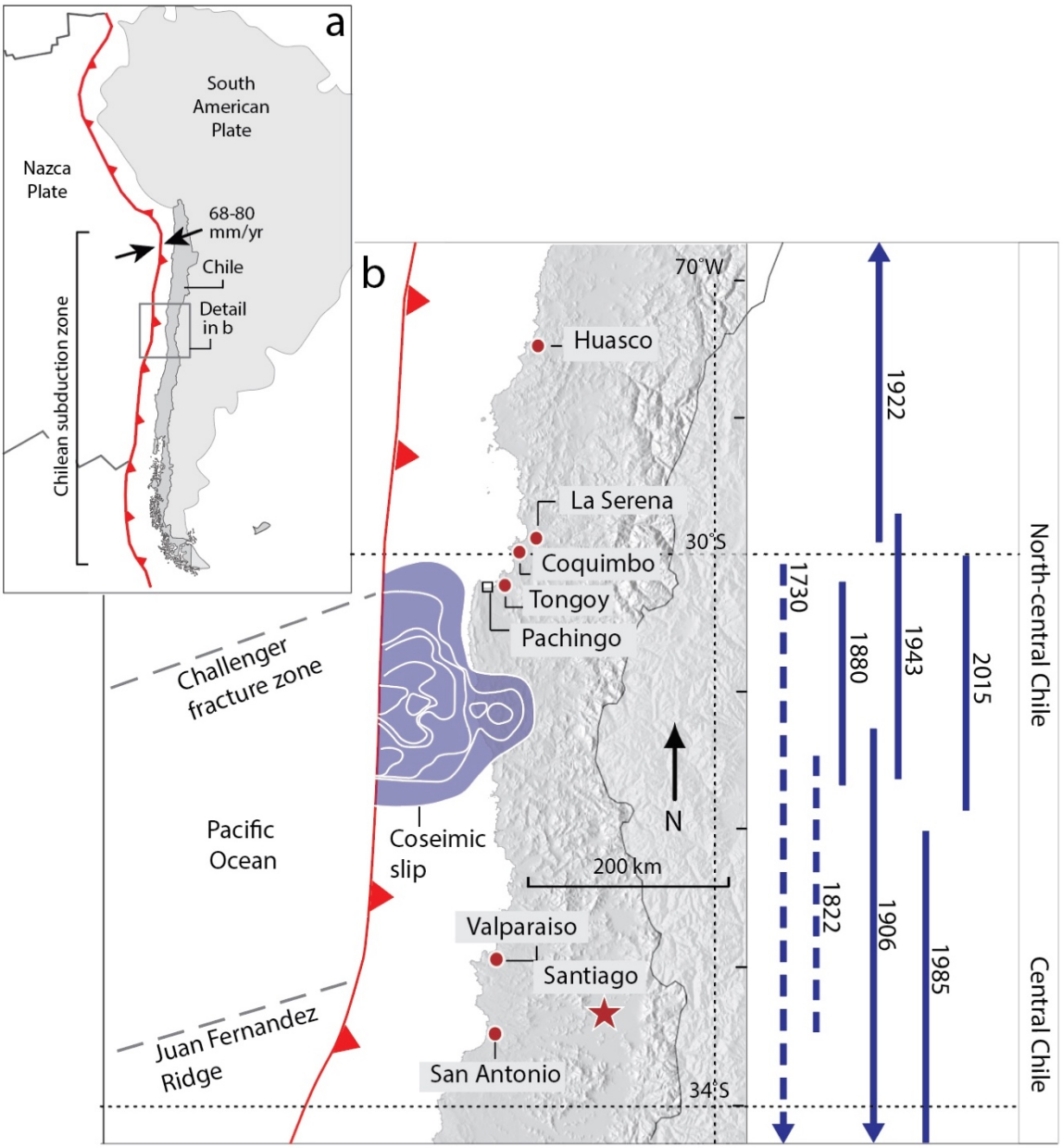

Figure 1. Index maps. a) Plate-tectonic setting of Chile in western South America. b) Location of the study area in north-central Chile, main tectonic features, and estimated rupture lengths of the largest historical earthquakes in central and north-central Chile since 1730 shown by dashed lines where inferred and solid lines where measured. Ruptures compiled from Lomnitz (1970), Comte et al. (1986), Beck et al. (1998), and Melnick et al. (2009), Udías et al. (2012), Melnick et al. (2012), and Cisternas et al. (2017). The 2015 north-central Chile earthquake slip distribution is pictured offshore in purple from Barnhart et al. (2016).

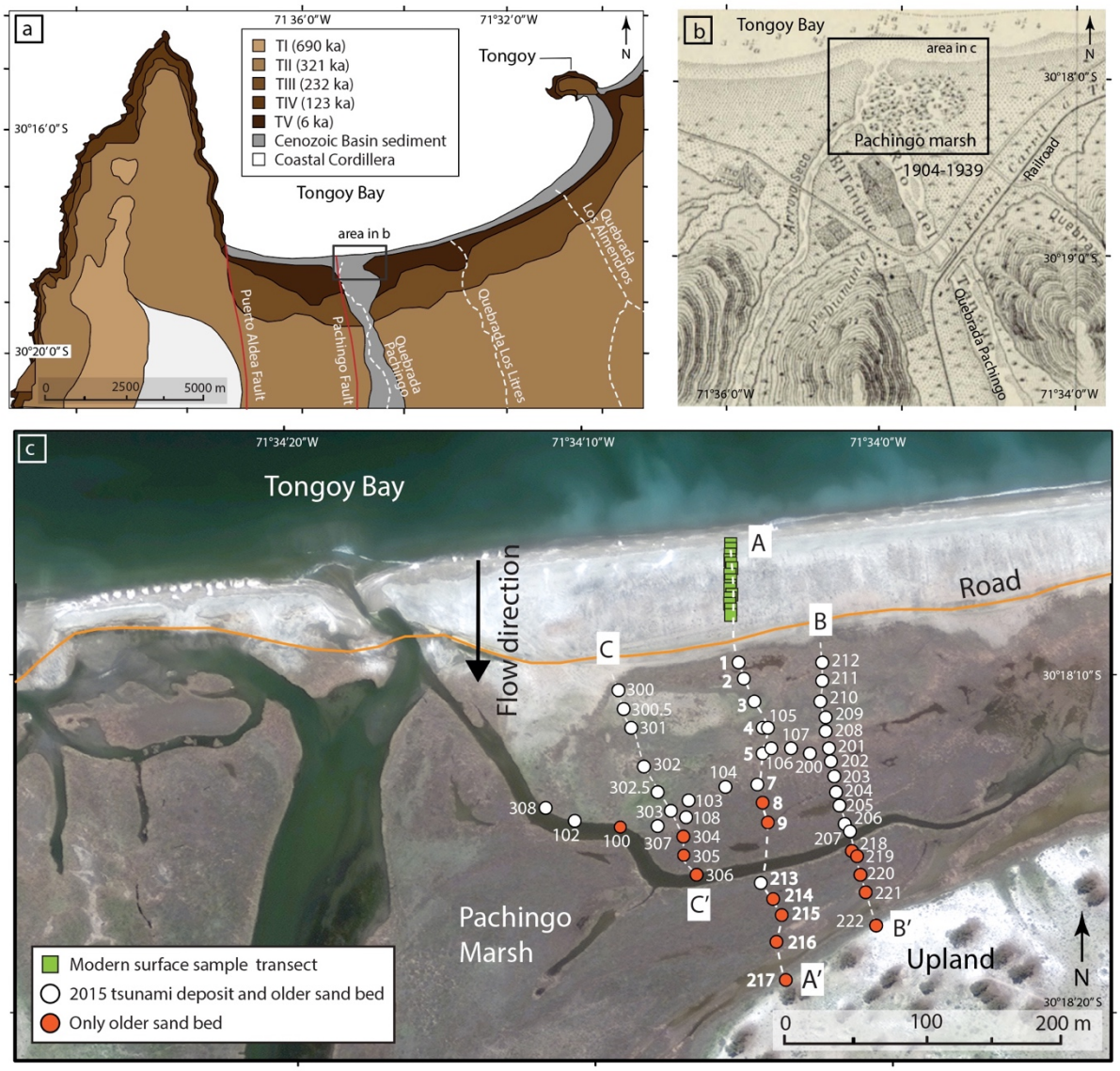

Figure 2. a) Tongoy Bay and the Pachingo marsh located in north-central Chile <50 km south of the coastal town of Coquimbo. The marsh is bordered by Miocene-Holocene aged marine terraces (TV:6 ka; TIV: 123 ka; TIII: 232 ka; TII: 321 ka; TI: 690 ka; Ota and Paskoff, 1993; Saillard et al., 2009, May et al., 2013) b) Map of the Pachingo marsh from AD 1904-1939. The actual field site with sample locations (as shown in c) is marked by a black box. c) Satellite Google Earth Pro, 2014 DigitalGlobe imagery of the Pachingo marsh. The coastal road is highlighted with an orange line. Described and sampled locations were made in 3 coast perpendicular transects (A-A', B-B', C-C'), shown by white dashed lines. Green squares are indicating where modern beach sediments were sampled along the A-A' transect. Sample locations are labeled where the 2015 sand deposit and older sand bed are present (white cirlces) and where only the older sand bed is present (red circles).

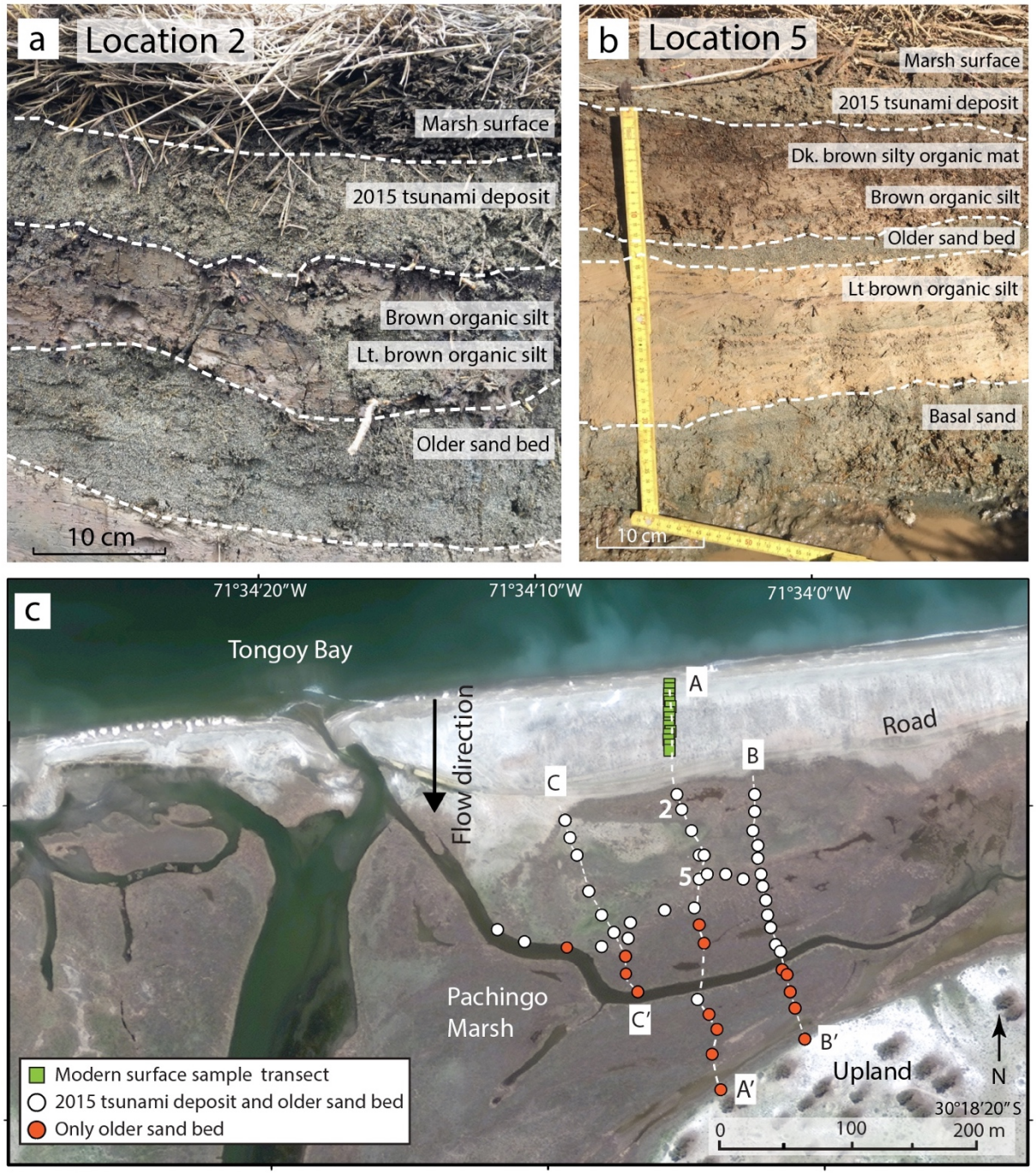

Figure 3. a) Photograph of sediments at location 2 along transect A-A' with generalized stratigraphy labeled. Unit contacts are outlined in dashed white lines. Rooted, dense, *Salicornia* sp. marks the top of the stratigraphy labeled "Marsh surface". b.) Photograph of sediments at location 5 along transect A-A' in the Pachingo marsh with generalized stratigraphy labeled. Unit contacts are outlined in dashed white lines. Dense, flattened *Salicornia* sp. can be seen at the top of the stratigraphy. c.) Site map showing the sample locations within the Pachingo marsh. Locations 2 and 5 along transect A-A' are labeled and bolded in white to mark where photographs in a and b were taken.

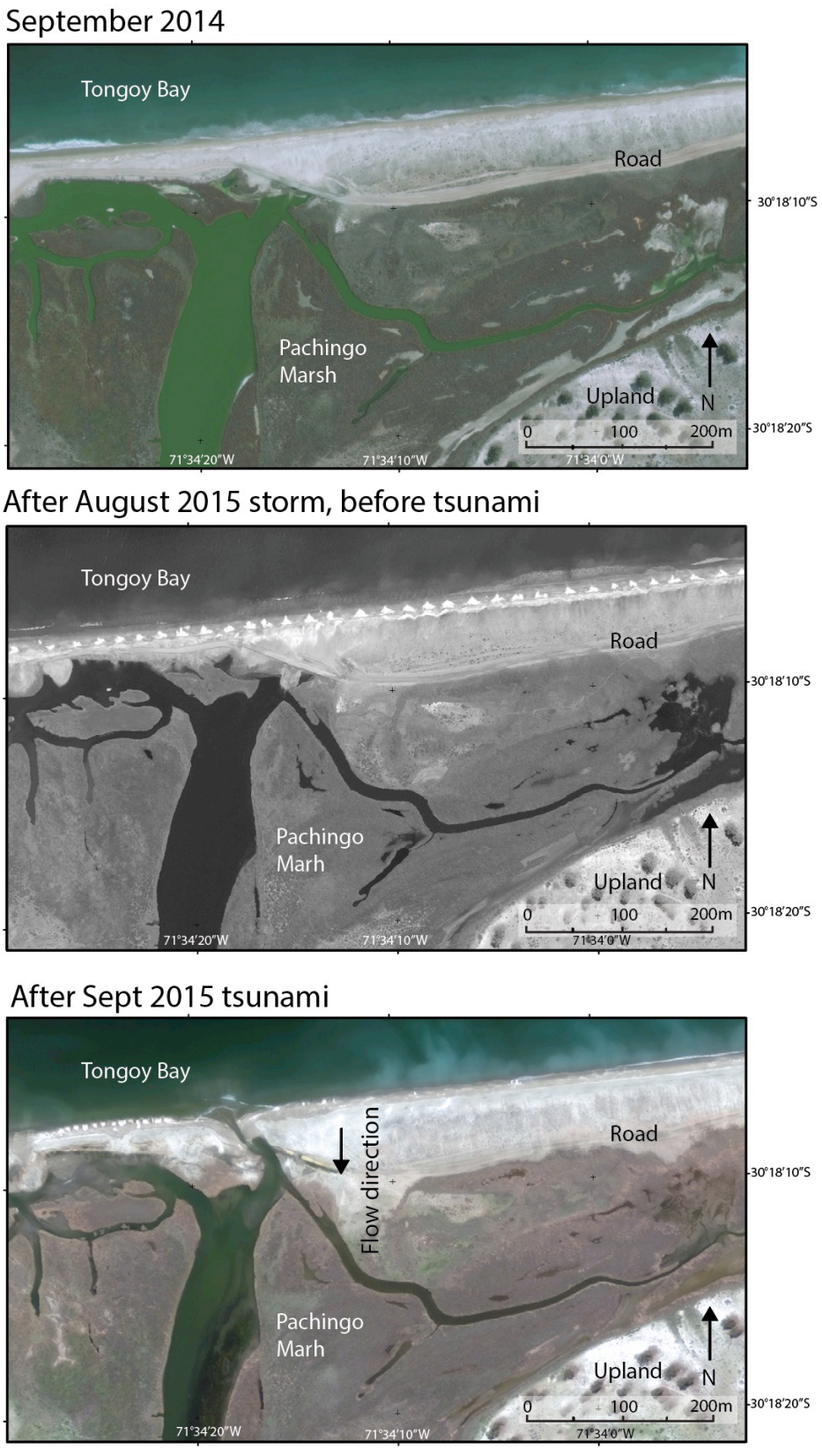

Figure 4. Satellite Google Earth Pro, 2014 DigitalGlobe imagery of the Pachingo marsh on September 2014 (top), after the August 2015 large storm surge (middle), and after the September 2015 tsunami (bottom).

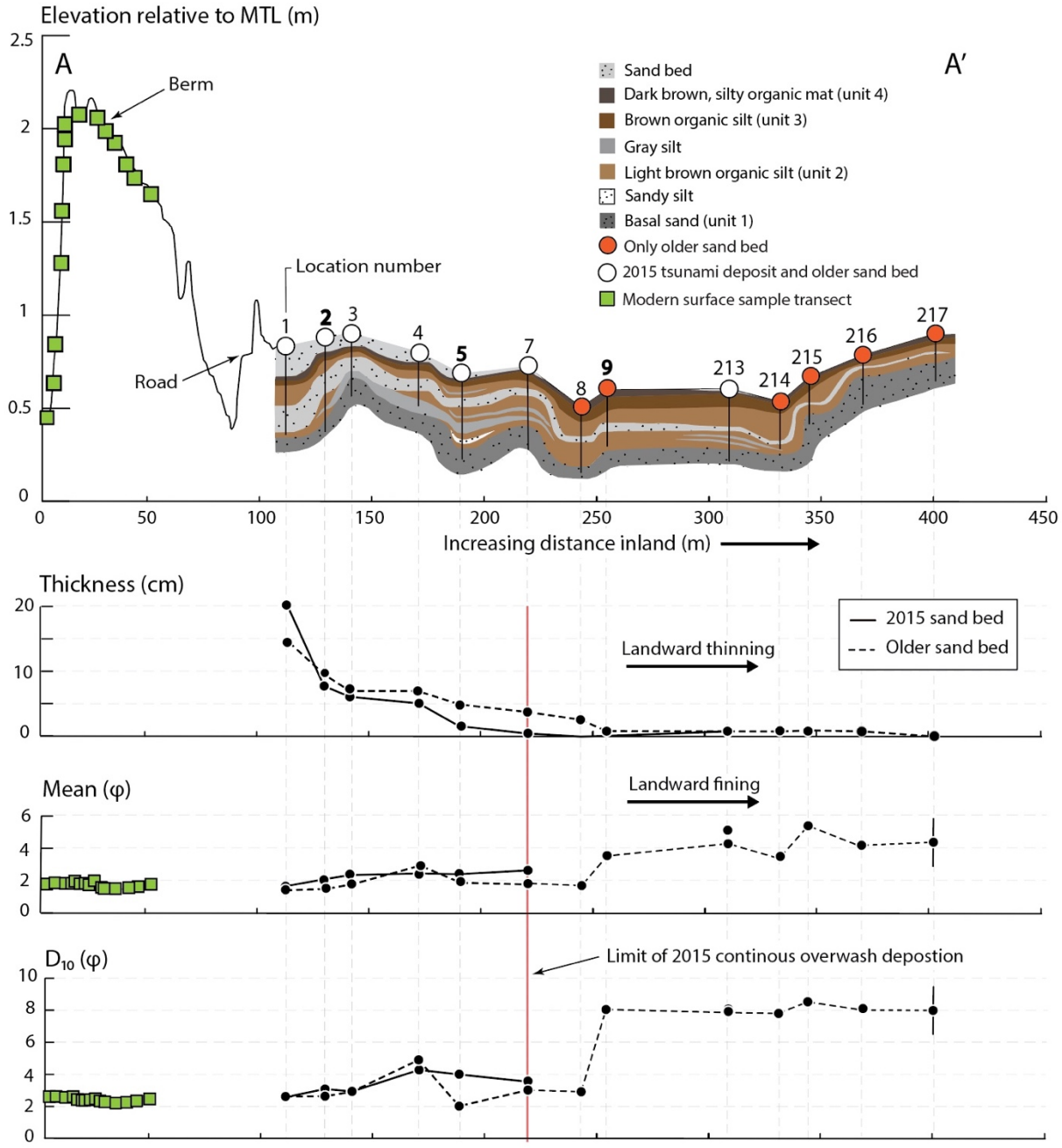

Figure 5. Coast perpendicular elevation profile along transect A-A' (see Fig. 2 for profile location) with detail of the Pachingo marsh stratigraphy. Sample locations along the transect are labeled and locations chosen for detailed analysis (2, 5, and 9) are bolded. Locations where the 2015 tsunami deposit and the older sand bed are present in stratigraphy (white circles) and locations where only the older sand bed is present (red circles) are marked. Modern sediment surface samples are shown with green squares. The beach berm and coastal road are labeled. Elevations are relative to mean tidal level (MTL). Thickness of deposit (cm), mean grain size (in phi), and D10 (diameter at which 10% of a sample's mass is comprised of smaller grains) are plotted for both the 2015 sand bed (solid line) and older sand bed (dashed line). The red, solid, vertical line depicts the inland extent of the 2015 tsunami continuous overwash deposition.

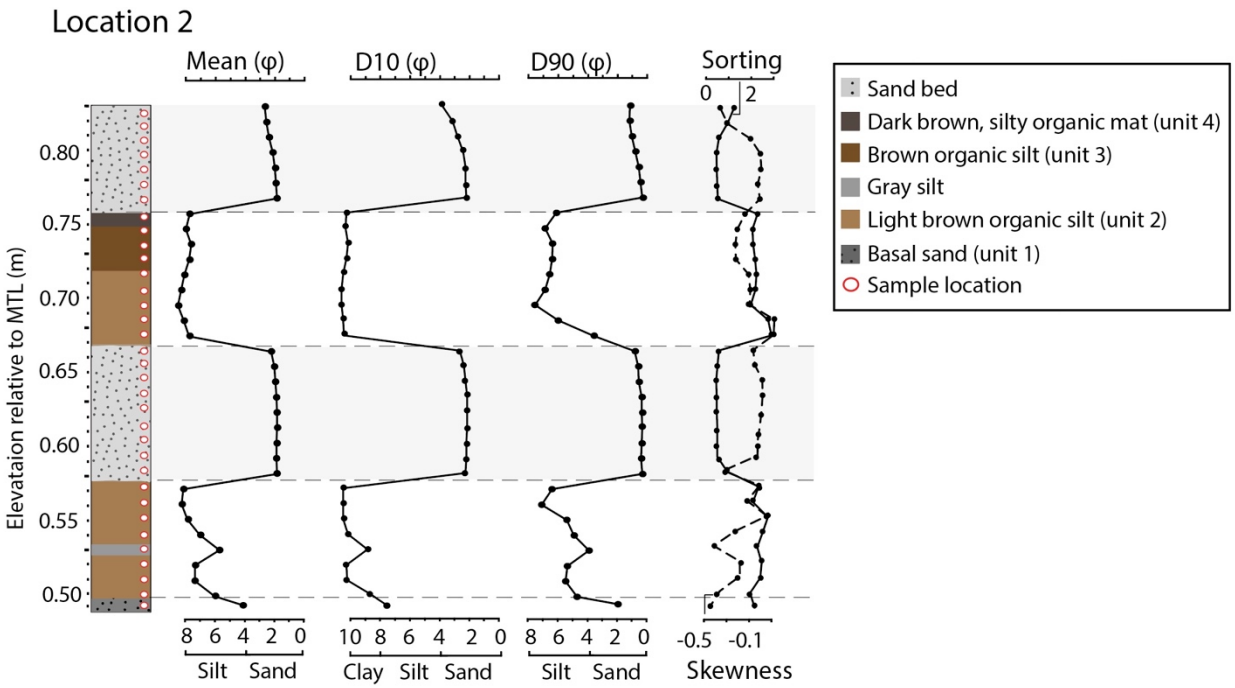

Figure 6. Stratigraphic column at location 2 depicting sedimentary units. White circles with red outlines indicate where high-resolution samples were taken for grain size. Plots show values of mean grain size, D10 (diameter at which 10% of a sample's mass is comprised of smaller grains), and D90 (diameter at which 90% of a sample's mass is comprised of smaller grains) at each sampling location through the stratigraphy. The 2015 tsunami deposit and older sand bed are shaded with light gray.

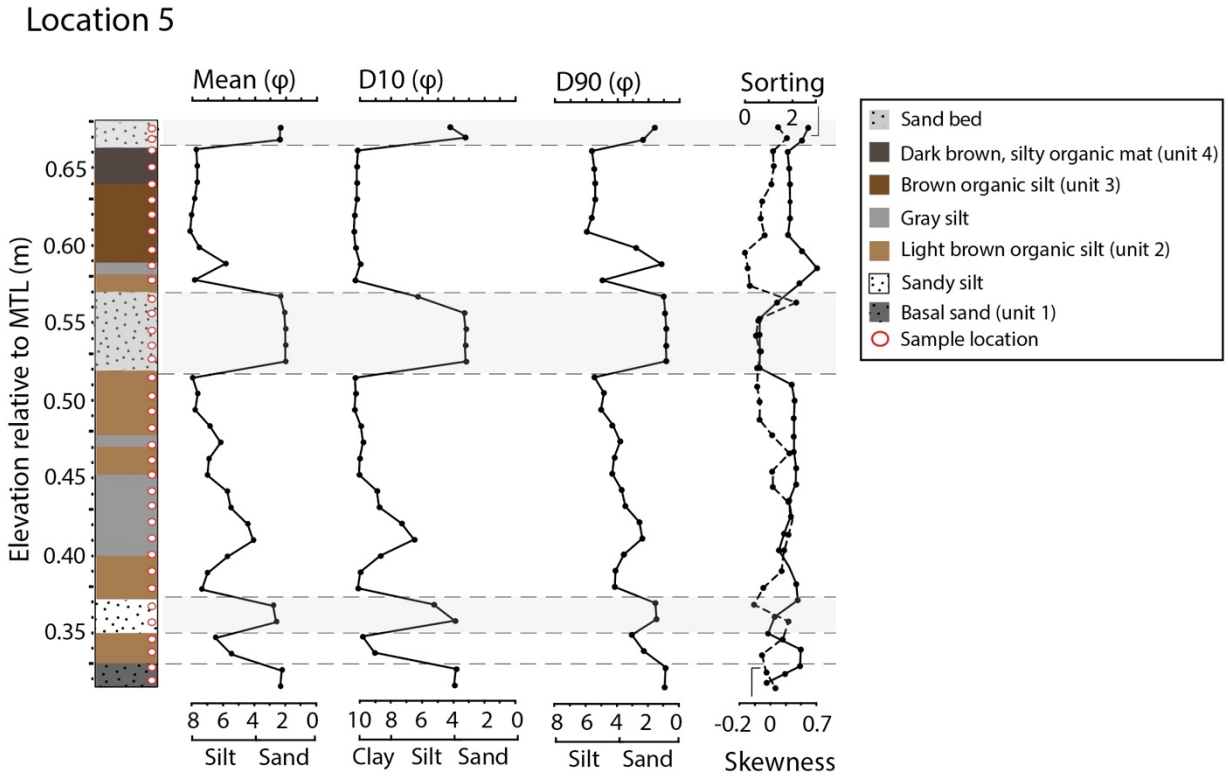

Figure 7. Stratigraphic column at location 5 depicting sedimentary units. White circles with red outlines indicate where high-resolution samples were taken for grain size. Plots show values of mean grain size, D10 (diameter at which 10% of a sample's mass is comprised of smaller grains), and D90 (diameter at which 90% of a sample's mass is comprised of smaller grains) at each sampling location through the stratigraphy. The 2015 tsunami deposit and older sand bed are shaded with light gray.

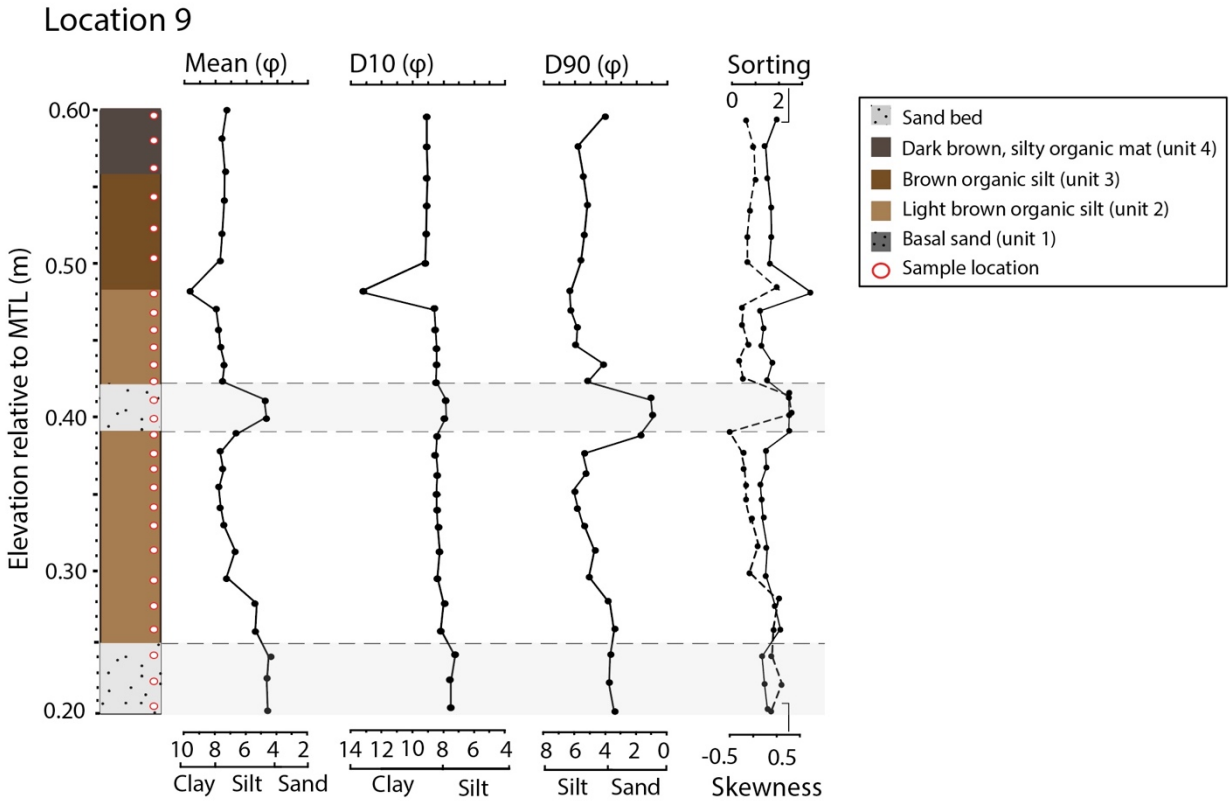

Figure 8. Stratigraphic column at location 9 depicting sedimentary units. White circles with red outlines indicate where high-resolution samples were taken for grain size. Plots show values of mean grain size, D10 (diameter at which 10% of a sample's mass is comprised of smaller grains), and D90 (diameter at which 90% of a sample's mass is comprised of smaller grains) at each sampling location through the stratigraphy. The depth range of the 2015 tsunami deposit and older sand bed are shaded with light gray.

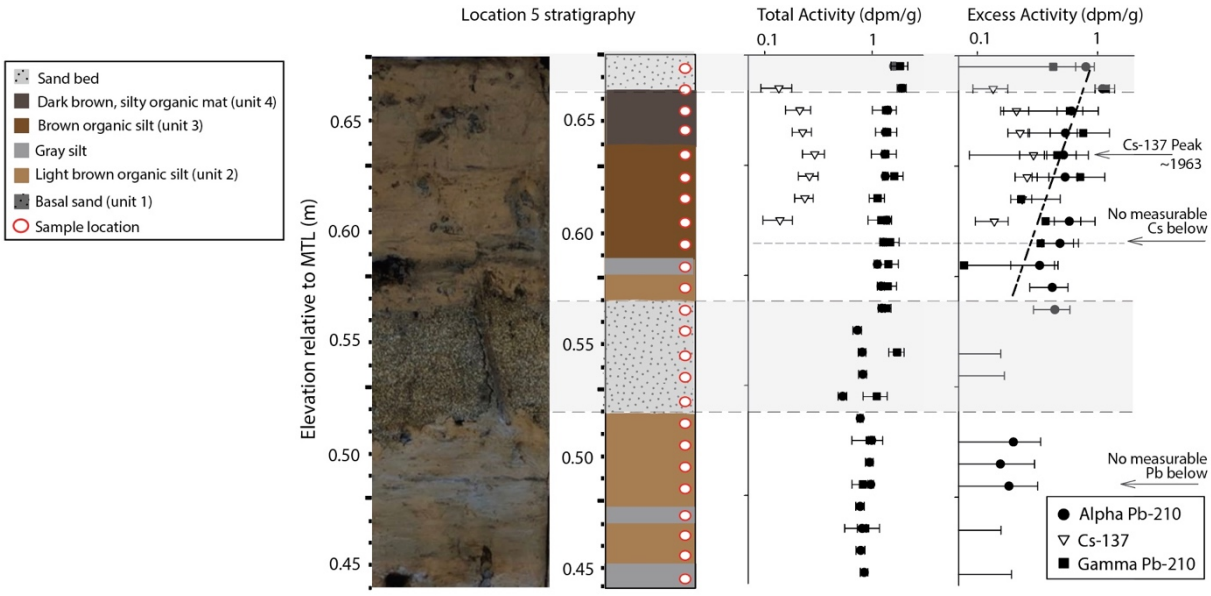

Figure 9. Photograph of the monolith from location 5 used for dating, stratigraphic column of sedimentary units from location 5, total activity (dpm/g), and excess activity (dpm/g). Values of alpha Pb^{210} (black circles), gamma Pb^{210} (black squares), and Cs^{137} (white triangles) are plotted. The Cs^{137} peak is labeled with an arrow depicting where the peak fallout of cesium (indicating the year 1963) is located in the stratigraphy. An arrow pointing to the end of alpha Pb^{210} data is also labeled. A labeled horizontal dashed black line indicates where there are no Cs^{137} values (below ~0.60 m MTL). The depth range of the 2015 tsunami deposit and older sand bed are shaded with light gray.

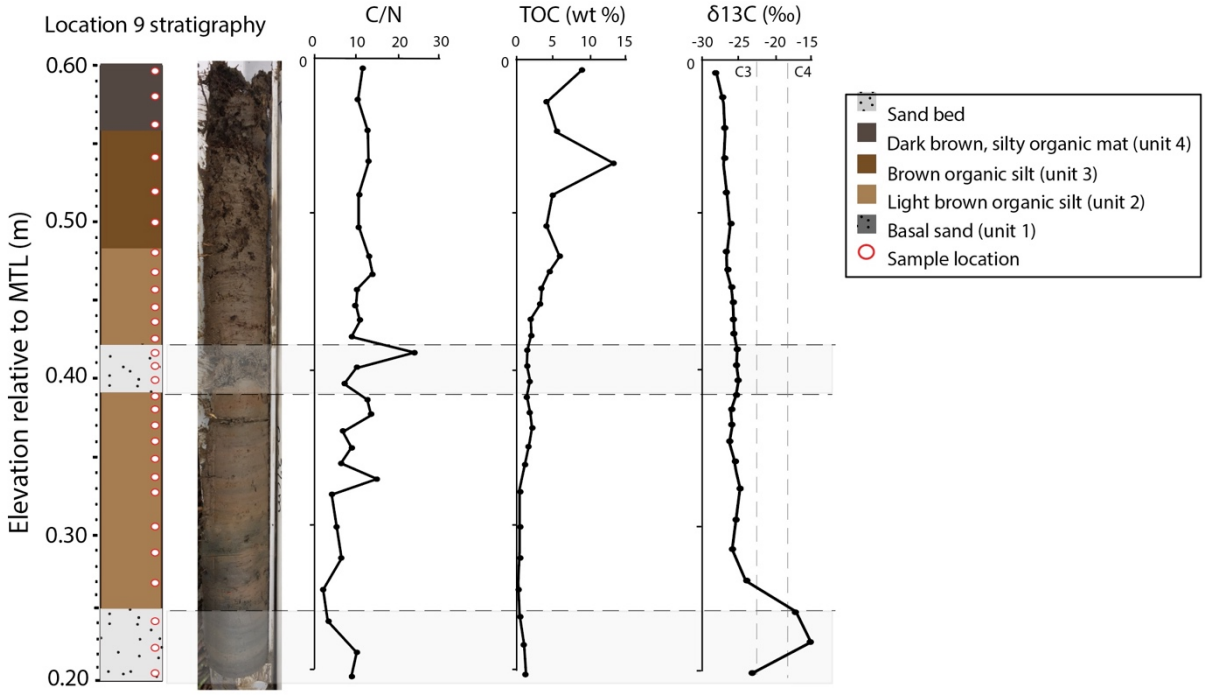

Figure 10. Photograph of the core from location 9 used for geochemical analysis, stratigraphic column of sedimentary units from location 9, organic carbon to total nitrogen ratio (C/N) plot, total organic carbon (TOC) plot, and $\delta^{13}C$ plot.

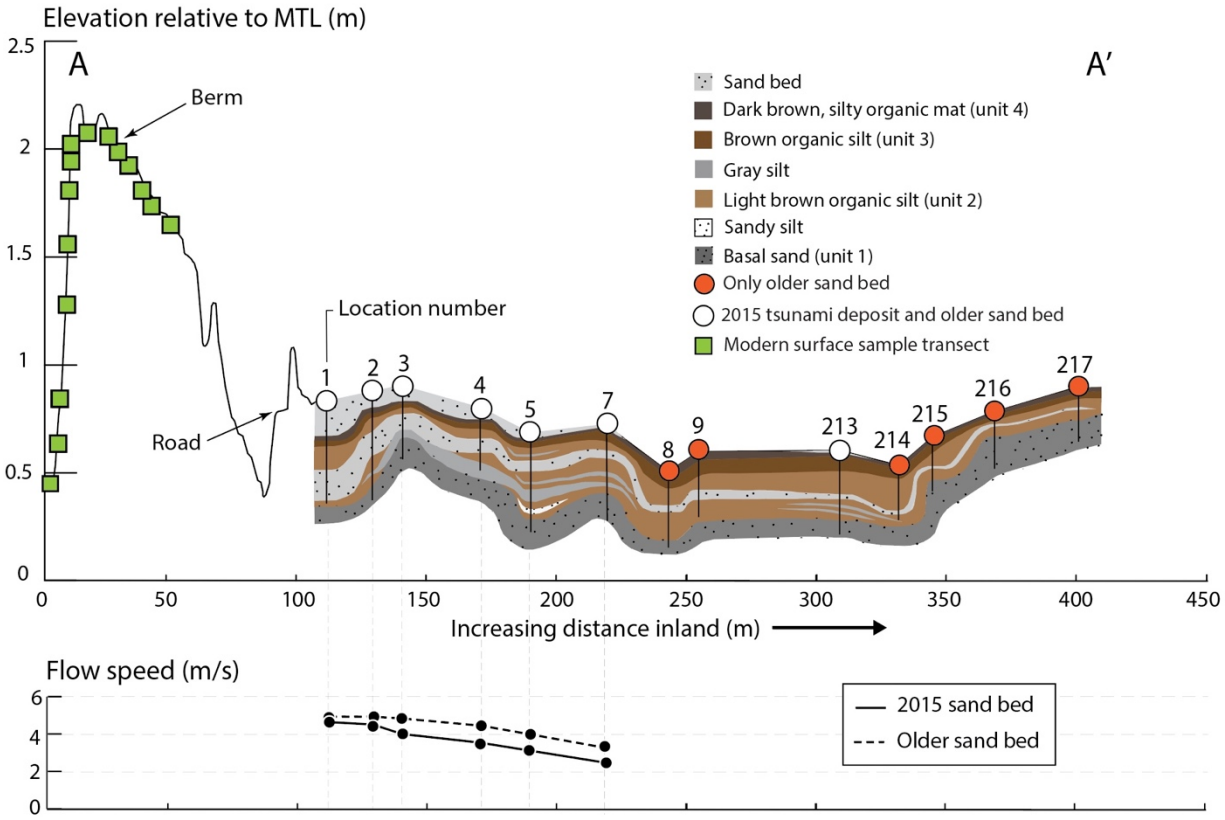

Figure 11. Coast perpendicular elevation profile along transect A-A' (see Fig. 2 for profile location) with detail of the Pachingo marsh stratigraphy. Sample locations along the transect are labeled and locations chosen for detailed analysis (2, 5, and 9) are bolded. Locations where the 2015 tsunami deposit and older sand bed are present in stratigraphy (white circles) and locations where only the older sand bed is present (red circles) are marked at the surface. Modern beach surface samples are shown with green squares. The beach berm and coastal road are labeled. Elevations are relative to mean tidal level (MTL). Flow speed results using locations 1, 2, 3, 4, 5, and 7 from transect A-A' are plotted for both the 2015 tsunami deposit (solid line) and the older sand bed (dashed line).

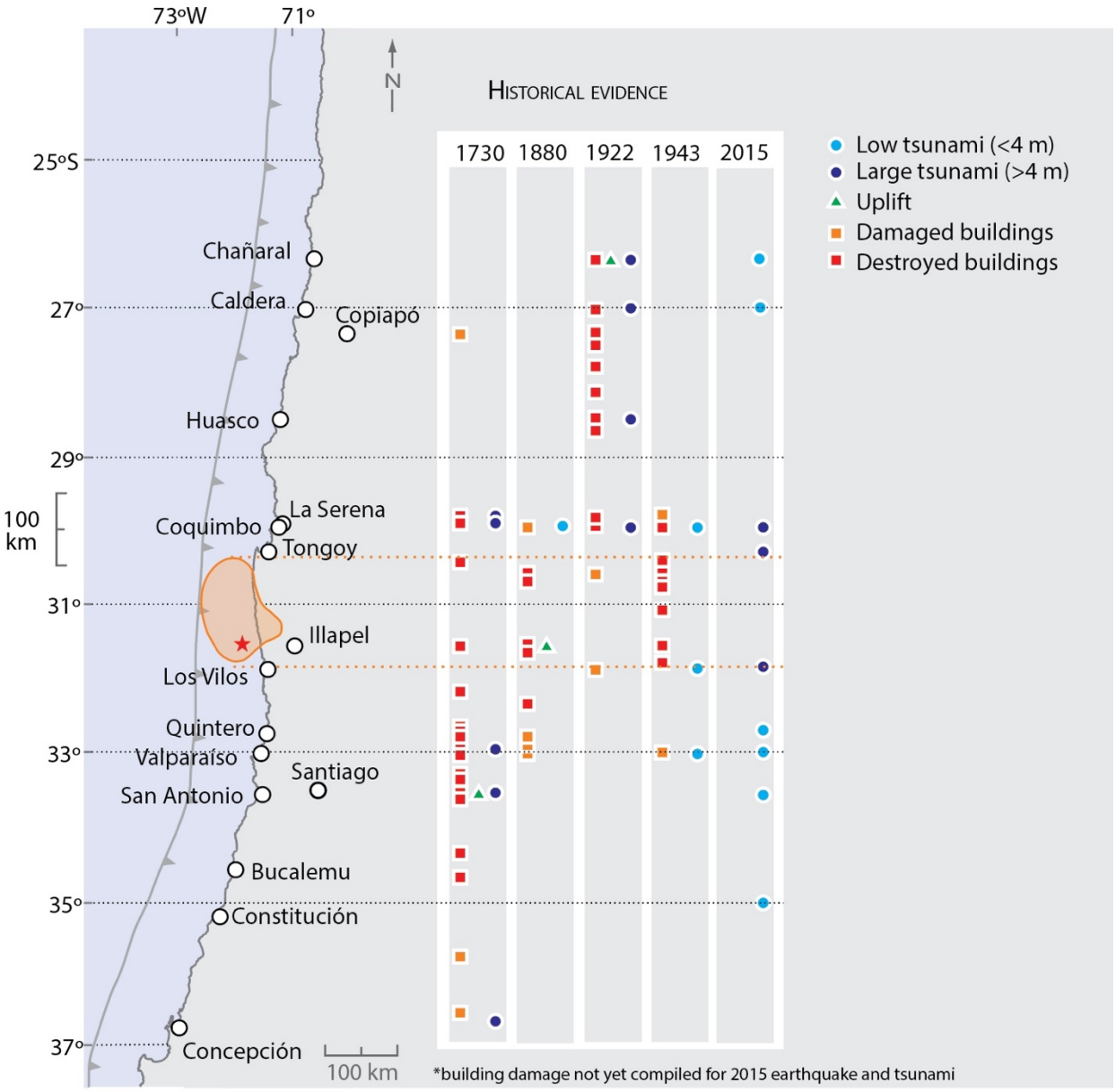

Figure 12. Summary of historical and paleoseismic evidence for ruptures along the north-central portions of the subduction zone over the last ~300 years. Symbols represent historical accounts of damage, uplift, or tsunami height from each of the events. Squares represent damaged (orange) and destroyed (red) buildings, triangle represents uplift, and circle represents lesser (light blue) and larger (dark blue) tsunami run-up measurements at different coastal locations. Historical records summarized by Lomnitz (1970), Cisternas et al. (2005, 2017), and Udías et al. (2012).

Table 1. Mean grain size of 2015 tsunami deposit and older sand bed for each sample location.

Location name	Latitude	Longitude	2015 tsunami deposit thickness (cm)	2015 tsunami deposit mean grain size (phi)	Older sand bed thickness (cm)	Older sand bed mean grain size (phi)
Transect A-A'						
1	30 18 9.72 S	71 34 5.232 W	20	1.798	14	1.729
2	30 18 10.332 S	71 34 5.016 W	7	2.066	10	1.797
3	30 18 10.656 S	71 34 4.944 W	6	2.289	7	1.910
4	30 18 11.556 S	71 34 4.332 W	5	2.237	7	2.80
5	30 18 12.143 S	71 34 4.352 W	1.5	2.273	5	1.962
7	30 18 13.097 S	71 34 4.553 W	0.5	2.546	4	1.963
8	30 18 13.788 S	71 34 4.332 W	< 0.5	--	3	1.810
9	30 18 14.184 S	71 34 4.188 W	< 0.5	--	1	3.732
213	30 18 16.027 S	71 34 4.389 W	1	4.896	1	4.247
214	30 18 16.649 S	71 34 3.990 W	--	--	1	3.787
215	30 18 16.980 S	71 34 3.689 W	--	--	1	5.422
216	30 18 17.734 S	71 34 3.883 W	--	--	1	4.103
217	30 18 18.811 S	71 34 3.545 W	--	--	< 0.5	--
Transect B-B'						
200	30 18 12.179 S	71 34 2.718 W	2	2.299	5	1.51
201	30 18 12.108 S	71 34 2.104 W	1	2.338	6	1.770
202	30 18 12.479 S	71 34 2.011 W	0.5	3.380	5.5	1.659
203	30 18 12.960 S	71 34 1.925 W	0.5	3.452	3	1.738
204	30 18 13.345 S	71 34 1.838 W	0.5	5.476	2	1.841
205	30 18 13.712 S	71 34 1.761 W	0.5	5.345	3	2.482
206	30 18 14.377 S	71 34 1.570 W	--	--	3	2.679
207	30 18 14.613 S	71 34 1.432 W	--	--	2	1.908
208	30 18 11.632 S	71 34 2.218 W	2	2.071	3	1.645
209	30 18 11.283 S	71 34 2.216 W	3	2.112	0.5	4.440
210	30 18 10.778 S	71 34 2.380 W	8	1.706	13	1.469
211	30 18 10.089 S	71 34 2.311 W	14	1.803	10	1.488
212	30 18 9.707 S	71 34 2.329 W	13	1.464	15	1.723
218	30 18 15.152 S	71 34 1.303 W	--	--	5	3.579
219	30 18 15.329 S	71 34 1.206 W	--	--	--	--
220	30 18 15.898 S	71 34 1.059 W	--	--	1	3.201
221	30 18 16.331 S	71 34 0.880 W	--	--	< 0.5	--
222	30 18 17.359 S	71 34 0.519 W	--	--	0.5	--
Transect C-C'						
300	30 18 10.348 S	71 34 9.247 W	10	1.586	10	1.363
300.5	30 18 10.962 S	71 34 9.054 W	7	1.820	5	1.563
301	30 18 11.413 S	71 34 8.800 W	3	1.971	6	1.341
302	30 18 12.608 S	71 34 8.386 W	3	5.980	3	1.668
303	30 18 13.899 S	71 34 7.470 W	< 0.5	--	1	2.136
304	30 18 14.655 S	71 34 7.085 W	--	--	1	3.571
305	30 18 15.185 S	71 34 6.820 W	--	--	1	2.960
306	30 18 15.802 S	71 34 6.606 W	--	--	2	2.104
307	30 18 14.353 S	71 34 7.934 W	--	--	1	2.059

Table 2. Comparison of sedimentary characteristics between the 2015 tsunami deposit and the older sand bed.

	2015 tsunami deposit	Older sand bed
Tsunami criteria		
Laterally continuous deposit (>200 m inland)	✓	✓
Upward fining	✓	✓
Landward fining	✓	✓
Landward thinning	✓	✓
Sharp or erosive lower contact (<1-3 mm)	✓	✓
Similar in composition to modern samples	✓	✓
Sand bed characteristics		
Coarsest grain size (phi)	1.8	1.7
Overwash sediment inland extent (m)	~225	~400
Maximum bed thickness (cm)	20	15
Flow speed at location 1 (m/s)	4.7	4.8
Flow speed at location 7 (m/s)	2.5	3.6